Available online at www.sciencedirect.com
ScienceDirect
Comput. Methods Appl. Mech. Engrg. 364 (2020) 112928
Computer methods in applied mechanics and engineering
www.elsevier.com/locate/cma

Stochastic isogeometric analysis in linear elasticity☆

Ramin Jahanbin*,[1], Sharif Rahman[2]

College of Engineering, The University of Iowa, Iowa City, IA 52242, USA

Received 24 June 2019; received in revised form 7 November 2019; accepted 12 February 2020
Available online xxxx

Abstract

A new stochastic method, integrating spline dimensional decomposition (SDD) and isogeometric analysis (IGA), is proposed for solving stochastic boundary-value problems from linear elasticity. The method, referred to as SDD–IGA, involves Galerkin isogeometric analysis as a deterministic solver for governing partial differential equations and a novel Fourier-like orthogonal spline expansion generated from the analysis-of-variance decomposition of a high-dimensional function. For the stochastic part of the SDD–IGA method, an innovative dimension-reduction integration technique is presented for efficiently calculating the expansion coefficients. Analytical formulae have been derived to calculate the second-moment properties of an SDD–IGA approximation for a general output random variable of interest. Numerical examples demonstrate the capability of a low-order SDD–IGA in efficiently delivering probabilistic solutions with an approximation quality as good as, if not better than, that obtained from a high-order polynomial dimensional decomposition. The proposed SDD–IGA method is most suitable in the presence of locally nonlinear or nonsmooth behavior commonly found in applications.

Keywords: Uncertainty quantification; Isogeometric analysis; ANOVA; Computational stochastic mechanics; Karhunen–Loève expansion

1. Introduction

Design and analysis of almost all mechanical systems involve uncertainties in external loads, boundary conditions, material properties, and geometry. In many cases, these uncertainties need to be propagated to a response variable of interest via solution of stochastic partial differential equations (PDEs). Analytical and numerical methods have been progressively studied in this field of research to model the statistical characteristics of the response. Naive direct sampling methods, such as Monte Carlo simulation (MCS) [1,2], are most versatile. One major drawback of MCS, though, is its slow convergence rate, which makes the procedure costly, if not prohibitive, even though convergence is almost assured. Moreover, the rate of convergence does not depend on the dimension of the stochastic domain, which is intriguing in the case of high-dimensional problems. On the other hand, the illustrious stochastic finite element methods (SFEMs) [3,4] have been proposed as powerful computational tools to solve stochastic PDEs, mostly in the context of linear elasticity. The Galerkin approaches [5,6] based on variational forms often

☆ Grant sponsor: U.S. National Science Foundation; grant number: CMMI-1607398.
* Corresponding author.
E-mail address: ramin-jahanbin@uiowa.edu (R. Jahanbin).
[1] Ph.D. student.
[2] Professor of mechanical engineering.

https://doi.org/10.1016/j.cma.2020.112928
0045-7825/

provide very accurate results but are expensive. Regression methods [7] have been established to reduce the cost, but lower accuracy is generally expected. Perturbation methods [8,9], spectral decomposition methods [10,11], and efficient non-intrusive sparse grids methods [12] are other popular approaches for solving stochastic PDEs along with the stochastic boundary element method [13,14]. One significant contribution of SFEM has been the integration of the uncertainty quantification (UQ) procedure into the classical finite element analysis (FEA). As a result, the applicability of FEA has surged tremendously. Furthermore, the stochastic meshfree method was introduced [15,16] to mitigate the low efficiency issues of past numerical schemes. In many cases, numerical analyses are carried out along with MCS to evaluate their accuracy whenever possible.

Polynomial chaos expansion (PCE) methods [17,18] are commonly used in UQ analysis. These methods, however, generally struggle when they encounter a large number of random variables as the number of expansion coefficients surges rapidly. This phenomenon is called the curse of dimensionality. In an effort to enhance the performance of globally supported PCE, domain decomposition techniques, such as multi-element formulation of PCE [19] and multi-element collocation methods [20], were introduced. The idea was to decompose the domain based on some variance error threshold. However, in the presence of many subdomains, the multi-element PCE becomes computationally inefficient. Although the latter helped with the efficiency issues, the functions were still only C^0-continuous at the element boundaries. Moreover, the method incorporated referential dimensional decomposition (RDD), also known as anchored decomposition, which was sub-optimal and would be inferior to analysis-of-variance (ANOVA) dimensional decomposition (ADD) [21]. More recent work on stochastic PDEs includes the spline fictitious boundary element method [22], collocation methods [23], and investigation of the multiscale aspects of randomness [24], where uncertainty may happen at different scales (macro, micro, and so forth). SFEMs often require a large number of function evaluations (FEA) [25]. That is why, in practice, they still need improvement in terms of computational consumption due to high mesh density [26]. Another compelling issue is the computational difficulties with high-dimensional problems in the stochastic domain, where multi-dimensional integrals are solved. Consequently, only direct sampling methods, such as MCS, might remain affordable. In this case, the dimension-reduction integration (DRI) technique [27] is a powerful tool to efficiently estimate the integrals involving high-dimensional functions.

Introduced to bridge the gap between computer-aided design (CAD) and FEA, isogeometric analysis (IGA) [28,29] exploits basis splines (B-splines) and non-uniform rational B-splines (NURBS) as basis functions that are globally smooth and are able to handle complex geometries elegantly [30,31]. This method is desirable in engineering applications as it preserves an exact representation of many geometrical or computational domains. Moreover, the convergence of the results is assured through mesh refinement [32]. Drawbacks of the watertight modeling for complex geometries have been alleviated by the generalization of NURBS into T-splines [33,34]. It is noteworthy that a major shortcoming of the existing Fourier-based UQ methods, such as PCE and polynomial dimensional decomposition (PDD) [35] methods, lies in the very nature of the polynomial basis functions employed. Orthogonal splines based on B-splines have been studied for least squares approximations [36]. The goal has been to harness the approximating power of B-splines. In the case of a nonsmooth or even heavily oscillatory random function, the limited control over the orthogonal polynomials becomes calamitous. An accurate solution, in this case, demands a significantly large polynomial degree. On the other hand, geometrical modeling error inherited by the classical FEA methods is a daunting disadvantage when a high accuracy in numerical simulation is desired. Oftentimes, these two factors join hands to make existing stochastic numerical methods provide unsatisfactory results. Consequently, as the IGA is now beginning to be widely used in computational mechanics, there is a need for expanding the applications of this method to the stochastic level in order to establish a stochastic isogeometric analysis (SIGA) framework, where all underlying analyses are conducted via B-splines or NURBS.

A few studies in conjunction with SIGA have been reported. They include analysis of functionally graded plates [37], spectral analysis of linear elasticity problems [38], and a stochastic collocation method [39] with the ultimate goal of structural design or safety assessments. In the work by Li et al. [38], the existing PCE method is exploited involving a globally supported polynomial basis for stochastic analysis, although B-splines and NURBS have been used for deterministic calculations. Due to the mismatch in the basis functions, the approximating power of SIGA has not been harnessed to its maximum level. Indeed, SIGA naturally inherits the desirable properties of B-splines and NURBS and satisfactorily handles smooth and nonsmooth functions, not only in the stress analysis and random field discretization, but also within the stochastic domain. Moreover, these methods are ill-equipped to deal with high-dimensional problems, because of the tensor-product structure mandated by PCE. Therefore,

new computational methods capable of exploiting low effective dimensions of high-dimensional functions are still desirable, and the authors envision attaining a higher accuracy by capitalizing on B-splines and/or NURBS, not only for deterministic computations, but also for subsequent stochastic analysis. This is the principal motivation for this work.

This paper presents a new stochastic method, coupling spline dimensional decomposition (SDD) and IGA for solving a general stochastic boundary-value problem from linear elasticity. While this paper addresses the computational and practical aspects of the method, referred to as SDD–IGA, readers looking for rigorous mathematical analysis of SDD, including theoretical results and their formal proofs, should check the companion paper [40].[3] The paper is organized as follows. Section 2 presents a description of random input and requisite assumptions, followed by the formulation of the stochastic boundary-value problem and its finite-dimensional approximation via the Galerkin method. The SDD method is formally presented in Section 3, including derivation of the output statistics from an SDD approximation. The SDD approximation is then coupled with the non-intrusive deterministic IGA framework to construct the stochastic method. Section 4 presents a DRI technique, customized for SDD, to alleviate the numerical difficulties of high-dimensional integration while calculating the expansion coefficients. Four numerical examples are provided in Section 5 to analyze the accuracy and efficiency of the proposed method and the effectiveness of DRI to evaluate various probabilistic response characteristics. Section 6 discusses the future outlook before the conclusions are drawn in Section 7. Appendices A through C explain or provide introductory basics of the isogeometric method, special cases of the SDD approximation, and additional details of the numerical examples.

2. Stochastic boundary-value problem

Let $\mathbb{N} := \{1, 2, \ldots\}$, $\mathbb{N}_0 := \mathbb{N} \cup \{0\}$, $\mathbb{R} := (-\infty, +\infty)$, and $\mathbb{R}_0^+ := [0, +\infty)$ represent the sets of positive integer (natural), non-negative integer, real, and non-negative real numbers, respectively. For a physical or spatial dimension $d = 1, 2, 3$, denote by $\mathcal{D}$ a closed bounded set of $\mathbb{R}^d$, which can represent a linear-elastic, deformable body under equilibrium. In stochastic analysis of a general linear-elasticity problem, which is the focus of this work, the applied loads, boundary conditions, material properties, and geometry, defined on or for $\mathcal{D}$, are likely to be uncertain due to their inherent statistical variability. This is referred to as the stochastic boundary-value problem or, simply, the stochastic problem in this work.

2.1. Input random variables and fields

For $N \in \mathbb{N}$ and $k = 1, \ldots, N$, define $\mathbb{A}^{\{k\}} := [a_k, b_k]$ as a finite closed interval, where $a_k, b_k \in \mathbb{R}$ and $b_k > a_k$. Then $\mathbb{A}^N := \times_{k=1}^N \mathbb{A}^{\{k\}} = \times_{k=1}^N [a_k, b_k]$ represents a closed bounded subdomain of $\mathbb{R}^N$, where $\times$ symbolizes tensor product. The domain $\mathbb{A}^N$ is referred to as the stochastic domain in this paper.

Let $(\Omega, \mathcal{F}, \mathbb{P})$ be a complete probability space, where Ω is a sample space representing an abstract set of elementary events, $\mathcal{F}$ is a σ-algebra on Ω, and $\mathbb{P} : \mathcal{F} \to [0, 1]$ is a probability measure. With $\mathcal{B}^N := \mathcal{B}(\mathbb{A}^N)$ representing the Borel σ-algebra on $\mathbb{A}^N \subseteq \mathbb{R}^N$, consider an $\mathbb{A}^N$-valued input random vector $\mathbf{X} := (X_1, \ldots, X_N)^T : (\Omega, \mathcal{F}) \to (\mathbb{A}^N, \mathcal{B}^N)$, describing the statistical uncertainties in all input and system parameters, including external loads, displacement boundary conditions, material properties, and geometry, of a mechanical system. The integer N, which represents the total number of input random variables, is often referred to as the dimension of the stochastic problem. As an example, consider a simply-supported beam with random length L, and random Young's modulus E, which is subjected to two vertically applied concentrated forces F_1 and F_2. If all of these input parameters are modeled as random variables, then $\mathbf{X} := (L, E, F_1, F_2)^T$ with stochastic dimension $N = 4$.

Denote by $F_{\mathbf{X}}(\mathbf{x}) := \mathbb{P}(\cap_{k=1}^N \{X_k \le x_k\})$ a joint distribution function of $\mathbf{X}$, admitting a joint probability density function (PDF) $f_{\mathbf{X}}(\mathbf{x}) := \partial^N F_{\mathbf{X}}(\mathbf{x}) / \partial x_1 \cdots \partial x_N$. Similarly, each random variable X_k is defined on the abstract marginal probability space $(\Omega^{\{k\}}, \mathcal{F}^{\{k\}}, \mathbb{P}^{\{k\}})$, comprising sample space $\Omega^{\{k\}}$, σ-algebra $\mathcal{F}^{\{k\}}$, and probability measure $\mathbb{P}^{\{k\}}$.

Depending on the stochastic problem, some of the input parameters may possess spatial variability, suggesting a need for their random field description. Common examples are elastic properties of engineering materials, size and

[3] The PDF file to this manuscript is available at http://user.engineering.uiowa.edu/~rahman/sdd.pdf.

shape characteristics of mechanical components, and wind and snow loads in structural systems, to name a few. For computational purposes, the random fields must be discretized into a finite number of constituent random variables. An oft-used approach entails the Karhunen–Loève (K–L) expansion [41], leading to an infinite series expansion of the random field consisting of deterministic functions of space and uncorrelated random variables.

Let $\alpha(\mathbf{z}, \cdot)$ be a real-valued random field with the physical coordinate $\mathbf{z}$ defined on $\mathcal{D} \in \mathbb{R}^d$, which has a *zero* mean and a square-integrable covariance function $\Gamma : \mathcal{D} \times \mathcal{D} \to \mathbb{R}$. Any of the input parameters described in the preceding paragraphs can be represented by this random field. Given an infinite sequence of eigenpairs $\{\lambda_i, \phi_i(\mathbf{z})\}_{i\in\mathbb{N}}$, obtained from solving the Fredholm integral equation

$$\int_{\mathcal{D}} \Gamma(\mathbf{z}, \mathbf{z}')\phi(\mathbf{z}')d\mathbf{z}' = \lambda\phi(\mathbf{z}), \tag{1}$$

the random field admits a mean-square convergent infinite series expansion [41]

$$\alpha(\mathbf{z}, \cdot) \sim \sum_{i=1}^{\infty} \sqrt{\lambda_i}\phi_i(\mathbf{z})X_i,$$

where $\{X_i\}_{i\in\mathbb{N}}$ is an infinite sequence of *zero*-mean, standardized, uncorrelated random variables. In a practical setting, though, an N'-term truncation or K–L approximation, such as

$$\alpha_{N'}(\mathbf{z}, \cdot) = \sum_{i=1}^{N'} \sqrt{\lambda_i}\phi_i(\mathbf{z})X_i \tag{2}$$

of $\alpha(\mathbf{z}, \cdot)$, must be used, provided that the eigenvalues have been arranged in a descending sequence. The value of $N' \in \mathbb{N}$ is frequently selected from the condition that all truncated modes have *zero* or negligible contributions to the expansion. According to (2), the statistical variation of random field $\alpha(\mathbf{z}, \cdot)$ is being swapped with those controlled by N' uncorrelated random variables $X_1, \ldots, X_{N'}$. Other random field expansions or approximations comprising random variables are possible. Having said this, the K–L approximation has an error-minimizing property — a desirable optimal property recognized in the stochastic community.

The success of the K–L approximation is heavily reliant on the efficient solution of (1). For complex geometries in high dimensions, solving this eigenvalue problem is computationally intensive, where the eigensolutions must be obtained numerically. In the past, finite element method (FEM) [3] or mesh-free modeling [16] was employed to deliver such numerical solutions. More recent works are premised on Galerkin isogeometric [42] and isogeometric collocation methods [43], where the latter, by eliminating one dimension-order of domain integration, offers a hefty computational advantage over the former. Readers interested in further detail are directed to the aforementioned works.

In summary, the randomness in the stochastic problem may stem from spatially invariant random variables alone, from the discretization of spatially variant random fields, or both. If the stochastic problem contains spatially invariant random variables and random fields, then N represents the total number of random variables.

2.2. Assumptions

A set of conditions enforced on the input random variables is as follows.

Assumption 1. The input random vector $\mathbf{X} := (X_1, \ldots, X_N)^T : (\Omega, \mathcal{F}) \to (\mathbb{A}^N, \mathcal{B}^N)$ satisfies all of the following conditions:

(*a*) Each input random variable $X_k : (\Omega^{\{k\}}, \mathcal{F}^{\{k\}}) \to (\mathbb{A}^{\{k\}}, \mathcal{B}^{\{k\}})$ has absolutely continuous marginal distribution function $F_{X_k}(x_k) := \mathbb{P}(X_k \le x_k)$ and continuous marginal density function $f_{X_k}(x_k) := \partial F_{X_k}(x_k)/\partial x_k$ with a bounded support $\mathbb{A}^{\{k\}} \subset \mathbb{R}$.

(*b*) All component random variables $X_k, k = 1, \ldots, N$, are statistically independent, but not necessarily identical. Consequently, $\mathbf{X}$ is endowed with a product-type PDF, that is, $f_{\mathbf{X}}(\mathbf{x}) = \prod_{k=1}^{N} f_{X_k}(x_k)$, with a bounded support $\mathbb{A}^N \subset \mathbb{R}^N$.

(c) Given a non-negative integer $p_k \in \mathbb{N}_0$, each input random variable X_k possesses finite moments of all orders up to $2p_k$, that is, for all $k = 1, \ldots, N$ and $0 \le l \le 2p_k$,

$$\mathbb{E}\left[X_k^l\right] := \int_{\Omega} X_k^l(\omega) d\mathbb{P}(\omega) = \int_{\mathbb{A}^N} x_k^l f_{\mathbf{X}}(\mathbf{x}) d\mathbf{x} = \int_{\mathbb{A}^{\{k\}}} x_k^l f_{X_k}(x_k) dx_k < \infty,$$

where $\mathbb{E}$ is the expectation operator with respect to the probability measure $\mathbb{P}$ or $f_{\mathbf{X}}(\mathbf{x})d\mathbf{x}$.

Assumption 1 ensures the existence of a relevant sequence of orthogonal polynomials or splines consistent with the input probability measure. The discrete distributions and dependent variables are not considered in this paper.

According to Assumption 1, the probability measures of input random variables are defined on a closed, bounded domain. However, for those problems entailing unbounded domains, such as those emanating from normal and lognormal distributions, a measure transformation can be applied, so that all transformed variables are described on a bounded domain. This mapping, however, is not unique and likely leads to different orders of accuracy. In other words, a simple output function of normal random variables may become heavily nonlinear when transformed to uniform or other random variables. The bottom line is that the requirement for bounded probability measures is not prohibitive, as the distribution can be mapped onto a bounded domain, although at the cost of lower accuracy and/or efficiency. This will be addressed further in the numerical examples section.

2.3. Stochastic PDE

The governing equations of linear elasticity from the classical deterministic setting are easily generalized to the stochastic framework. Indeed, having an input random vector $\mathbf{X}$ defined in Section 2.1, whether or not it includes random variables from random field discretization, the stochastic PDE calls for finding the displacement vector $\mathbf{u}(\mathbf{z}; \mathbf{X})$ and stress vector $\boldsymbol{\sigma}(\mathbf{z}; \mathbf{X})$ solutions, which satisfy $\mathbb{P}$-almost surely

$$\begin{aligned} \nabla \cdot \boldsymbol{\sigma}(\mathbf{z}; \mathbf{X}) + \mathbf{b}(\mathbf{z}; \mathbf{X}) &= \mathbf{0} \quad \text{in } \mathcal{D}(\mathbf{X}) \subset \mathbb{R}^d, \\ \boldsymbol{\sigma}(\mathbf{z}; \mathbf{X}) \cdot \mathbf{n}(\mathbf{z}; \mathbf{X}) &= \bar{\mathbf{t}}(\mathbf{z}; \mathbf{X}) \quad \text{on } \Gamma_t(\mathbf{X}) \subset \partial\mathcal{D}(\mathbf{X}), \\ \mathbf{u}(\mathbf{z}; \mathbf{X}) &= \bar{\mathbf{u}}(\mathbf{z}; \mathbf{X}) \quad \text{on } \Gamma_u(\mathbf{X}) \subset \partial\mathcal{D}(\mathbf{X}), \end{aligned} \tag{3}$$

at every point $\mathbf{z} = (z_1, \ldots, z_d) \in \mathcal{D}(\mathbf{X}) \subset \mathbb{R}^d$ within the body such that

$$\Gamma_t(\mathbf{X}) \cup \Gamma_u(\mathbf{X}) \cup \Gamma_0(\mathbf{X}) = \partial\mathcal{D}(\mathbf{X}), \quad \Gamma_t(\mathbf{X}) \cap \Gamma_u(\mathbf{X}) = \emptyset,$$

with $\Gamma_0(\mathbf{X})$ representing the free boundary. Here, $\nabla := (\partial/\partial z_1, \ldots, \partial/\partial z_d)$ is a vector of gradients, $\mathbf{b}(\mathbf{z}; \mathbf{X})$ is the body force vector, $\bar{\mathbf{t}}(\mathbf{z}; \mathbf{X})$ is the prescribed traction vector, $\bar{\mathbf{u}}(\mathbf{z}; \mathbf{X})$ is the prescribed displacement vector, and $\mathbf{n}(\mathbf{z}; \mathbf{X})$ is an unit outward normal vector. The stress vector $\boldsymbol{\sigma}(\mathbf{z}; \mathbf{X})$ is obtained from $\mathbf{D}(\mathbf{z}; \mathbf{X}) : \boldsymbol{\epsilon}(\mathbf{z}; \mathbf{X})$, where $\mathbf{D}(\mathbf{z}; \mathbf{X})$ is the elasticity tensor and $\boldsymbol{\epsilon}(\mathbf{z}; \mathbf{X}) := (1/2)(\nabla + \nabla^T)\mathbf{u}(\mathbf{z}; \mathbf{X})$ is the strain vector. The symbols $\cdot$ and $:$ denote dot product and tensor contraction, respectively.

2.4. Finite-dimensional approximation

The first step to approximate the solution of (3) in a finite-dimensional space hinges on its variational or weak form. Denote by $L^2(\mathcal{D}(\mathbf{X}))$, the collection of all square integrable functions $\mathbf{u} : \infty \times \Omega \to \mathbb{R}^d$. Hence, the solution of the weak form resides in

$$\mathcal{U} := \left\{ \mathbf{u}(\mathbf{z}; \mathbf{X}) : \mathbf{u}(\mathbf{z}; \mathbf{X}) \in H^1(\mathcal{D}(\mathbf{X})), \mathbf{u}(\mathbf{z}; \mathbf{X}) \mid_{\Gamma_u} = \bar{\mathbf{u}}(\mathbf{z}; \mathbf{X}) \right\},$$

where $H^1(\mathcal{D}(\mathbf{X}))$ is the Sobolev space in which only the Dirichlet boundary conditions need to be satisfied. One major reason for transformation into the weak form is that it requires a lower derivative of the candidate solution function to exist and to be computed, which can make the numerical scheme more expedient and less strict on the regularity of the basis functions. The weighting functions are defined as

$$\mathcal{W} := \left\{ \mathbf{w}(\mathbf{z}; \mathbf{X}) : \mathbf{w}(\mathbf{z}; \mathbf{X}) \in H^1(\mathcal{D}(\mathbf{X})), \mathbf{w}(\mathbf{z}; \mathbf{X}) \mid_{\Gamma_u} = 0 \right\}.$$

Hence, the weak form is [30]

$$\mathcal{A}(\mathbf{u}(\mathbf{z}; \mathbf{X}), \mathbf{w}(\mathbf{z}; \mathbf{X})) = \mathcal{L}(\mathbf{w}(\mathbf{z}; \mathbf{X})), \tag{4}$$

where

$$\mathcal{A}(\mathbf{u}(\mathbf{z};\mathbf{X}),\mathbf{w}(\mathbf{z};\mathbf{X})) = \int_{\mathcal{D}(\mathbf{X})} \boldsymbol{\epsilon}^T(\mathbf{u}(\mathbf{z};\mathbf{X}))\mathbf{D}(\mathbf{z};\mathbf{X})\boldsymbol{\epsilon}(\mathbf{w}(\mathbf{z};\mathbf{X}))\, d\mathbf{z} \tag{5}$$

and

$$\mathcal{L}(\mathbf{w}(\mathbf{z};\mathbf{X})) = \int_{\mathcal{D}(\mathbf{X})} \mathbf{w}^T(\mathbf{z};\mathbf{X})\mathbf{b}(\mathbf{z};\mathbf{X})\, d\mathbf{z} + \int_{\Gamma_t(\mathbf{X})} \mathbf{w}^T(\mathbf{z};\mathbf{X})\, \bar{\mathbf{t}}(\mathbf{z};\mathbf{X})\, d\Gamma_t. \tag{6}$$

With a set of regularity conditions satisfied, the weak form (4) and the strong form (3) are analytically equivalent [44]. It is elementary to illustrate that there is a symmetry to the bilinear functional $\mathcal{A}(\cdot,\cdot)$ in (5), which is a desirable property for numerical implementation purposes. Moreover, note that the first integral in (6) is on the entire domain and the second integral is on the boundary where the traction $\bar{\mathbf{t}}(\mathbf{z};\mathbf{X})$ is applied.

2.4.1. Galerkin discretization

The Galerkin method reduces the original problem to finite-dimensional vector subspaces $\mathcal{U}^h \subset \mathcal{U}$ and $\mathcal{W}^h \subset \mathcal{W}$, where the approximate solution may be calculated through a linear combination of a set of linearly independent basis functions residing in $\mathcal{U}^h$ and $\mathcal{W}^h$. Then, for all $\mathbf{w}^h \subset \mathcal{W}^h$, the Galerkin method yields

$$\mathcal{A}(\mathbf{v}^h(\mathbf{z};\mathbf{X}),\mathbf{w}^h(\mathbf{z};\mathbf{X})) = \mathcal{L}(\mathbf{w}^h(\mathbf{z};\mathbf{X})) - \mathcal{A}(\mathbf{w}^h(\mathbf{z};\mathbf{X}),\bar{\mathbf{u}}^h(\mathbf{z};\mathbf{X})) \tag{7}$$

with an assumption that for a given function $\bar{\mathbf{u}}^h(\mathbf{z};\mathbf{X}) \in \mathcal{U}^h$ and $\bar{\mathbf{u}}^h(\mathbf{z};\mathbf{X})\,|_{\Gamma_u} = \bar{\mathbf{u}}(\mathbf{z};\mathbf{X})$, for every $\mathbf{u}^h(\mathbf{z};\mathbf{X}) \in \mathcal{U}^h$, there exists a unique $\mathbf{v}^h(\mathbf{z};\mathbf{X}) \in \mathcal{W}^h$ such that

$$\mathbf{u}^h(\mathbf{z};\mathbf{X}) = \mathbf{v}^h(\mathbf{z};\mathbf{X}) + \bar{\mathbf{u}}^h(\mathbf{z};\mathbf{X}).$$

A brief introduction to isogeometric analysis is provided in Appendix A, where the notations are also introduced. More specifically, it elaborates on the NURBS basis functions for any physical single-patch problem of dimension $d = 1, 2,$ or 3, whether they correspond to the stress analysis or the K–L expansion. It is noteworthy, however, that the random field discretization and the FEA are not necessarily restrained to the use of identical basis functions. Considering the general multivariate NURBS basis functions $\bar{\mathrm{R}}_{\mathbf{i},\mathbf{p},\boldsymbol{\Xi}}$ for a given multi-index set $\mathbf{i}$, order vector $\mathbf{p}$, and set of knot vectors $\boldsymbol{\Xi}$, the finite-dimensional approximation by dint of the Galerkin approach is at hand.

2.4.2. Matrix formulation

A matrix formulation of the problem can be developed from (7). The same sets of basis functions are employed from $\mathcal{U}^h$ and $\mathcal{W}^h$ in the classical Galerkin approach [44], which also define the geometry. Essentially, the projection to the NURBS space is carried out by first considering the NURBS functions $\bar{\mathrm{R}}_{\mathbf{i},\mathbf{p},\boldsymbol{\Xi}}$ for a given $\mathbf{i} := (i_{k_1},\ldots,i_{k_d}) \in \mathbb{N}^d$ as the basis function index set, the order vector $\mathbf{p} := (p_{k_1},\ldots,p_{k_d}) \in {\mathbb{N}_0}^d$, and the set of knot vectors $\boldsymbol{\Xi} := (\boldsymbol{\xi}_1,\ldots,\boldsymbol{\xi}_d)$ with $1 \le i_{k_l} \le n_{k_l}$ and $1 \le l \le d$. Note that n_k is referred to as the number of basis functions in coordinate direction $k = 1,\ldots,d$ and n_c is the total number of basis functions or control points. It is once again emphasized that the notations are all defined in Appendix A.

The weak form is hence projected to the NURBS space, yielding [30]

$$\mathbf{K}(\mathbf{X})\mathbf{d}(\mathbf{X}) = \mathbf{F}(\mathbf{X}), \tag{8}$$

where

$$K_{ij}(\mathbf{X}) = \mathcal{A}((\bar{\mathrm{R}}_{\mathbf{i}(i,d),\mathbf{p},\boldsymbol{\Xi}}(\mathbf{z});\mathbf{X}),(\bar{\mathrm{R}}_{\mathbf{j}(j,d),\mathbf{p},\boldsymbol{\Xi}}(\mathbf{z});\mathbf{X})),$$
$$F_i(\mathbf{X}) = \mathcal{L}((\bar{\mathrm{R}}_{\mathbf{i}(i,d),\mathbf{p},\boldsymbol{\Xi}}(\mathbf{z});\mathbf{X})).$$

Here, K_{ij} represents the (i,j)th and F_i stands for the ith component of $\mathbf{K}$ and $\mathbf{F}$. A NURBS basis function's index $\mathbf{i}$ is related to i and the physical problem's dimension d in the stiffness matrix and force vector assembly procedure. This, illustrated by $\mathbf{i}(i,d)$ in the subscript of $\bar{\mathrm{R}}$, determines the contribution of each component to the global stiffness matrix and force vector. For more detailed information on how to assemble $\mathbf{K}$ and $\mathbf{F}$, refer to Section 4 of the work of Cottrell et al. [30]. Thus, the vector $\mathbf{d}$ is sought by

$$\mathbf{d}(\mathbf{X}) = \mathbf{K}^{-1}(\mathbf{X})\mathbf{F}(\mathbf{X}).$$

Let $\mathcal{I}$ be the multi-index set of all basis functions that define the geometry, as presented in Appendix A. Now, denote by $\mathcal{I}_{\tilde{\mathbf{u}}} \subset \mathcal{I}$ the multi-index set of all non-zero basis functions on $\Gamma_u(\mathbf{X})$. Eventually, the ith component of the approximate solution $\mathbf{u}^h(\mathbf{z};\mathbf{X}) \in \mathcal{U}^h$ can be written as

$$u_i^h(\mathbf{z};\mathbf{X}) = \sum_{\mathbf{j}\in\mathcal{I}-\mathcal{I}_{\tilde{\mathbf{u}}}} \bar{\mathrm{R}}_{\mathbf{j},\mathbf{p},\boldsymbol{\Xi}}(\mathbf{z}) d_{\mathbf{j}_i}(\mathbf{X}) + \sum_{\mathbf{j}\in\mathcal{I}_{\tilde{\mathbf{u}}}} \bar{\mathrm{R}}_{\mathbf{j},\mathbf{p},\boldsymbol{\Xi}}(\mathbf{z}) \bar{u}_{\mathbf{j}_i}^h(\mathbf{X}), \tag{9}$$

where $d_{\mathbf{j}_i}$ is the ith component of $\mathbf{d}_{\mathbf{j}}$, which itself is the jth component of $\mathbf{d}(\mathbf{X})$. Moreover, the second term on the right-hand side of (9) is equivalent to the ith component of $\bar{\mathbf{u}}^h(\mathbf{z};\mathbf{X})$, with $\bar{u}_{\mathbf{j}_i}^h(\mathbf{X})$ being its expansion coefficients in terms of the basis functions $\bar{\mathrm{R}}_{\mathbf{j}(i,d),\mathbf{p},\boldsymbol{\Xi}}(\mathbf{z})$.

In (8), matrix $\mathbf{K}$ and vectors $\mathbf{F}$ and $\mathbf{d}$ are generally all random. The solution provided by (9) is referred to as the IGA solution in terms of displacements. With the displacements calculated, the projected (approximate) stress tensor is

$$\boldsymbol{\sigma}^h(\mathbf{z};\mathbf{X}) = \mathbf{D}(\mathbf{z};\mathbf{X})\boldsymbol{\epsilon}^h(\mathbf{z};\mathbf{X}), \tag{10}$$

where $\boldsymbol{\epsilon}^h(\mathbf{z};\mathbf{X}) := (1/2)(\boldsymbol{\nabla} + \boldsymbol{\nabla}^T)\mathbf{u}^h(\mathbf{z};\mathbf{X})$ is the projected strain tensor. The elasticity tensor $\mathbf{D}(\mathbf{z};\mathbf{X})$ is generally random as well, since the mechanical properties may be random due to the uncertainties in the manufacturing processes.

3. A spline dimensional decomposition

Given an input random vector $\mathbf{X} := (X_1,\ldots,X_N)^T : (\Omega,\mathcal{F}) \to (\mathbb{A}^N,\mathcal{B}^N)$ with known PDF $f_{\mathbf{X}}(\mathbf{x})$ on $\mathbb{A}^N \subset \mathbb{R}^N$, let $y(\mathbf{X}) := y(X_1,\ldots,X_N)$, a real-valued, measurable transformation on $(\Omega,\mathcal{F})$, define a stochastic response or output function of interest. It is common to assume that the function y belongs to a reasonably large function class, such as the Hilbert space

$$L^2(\Omega,\mathcal{F},\mathbb{P}) := \left\{ y : \Omega \to \mathbb{R} : \int_\Omega |y(\mathbf{X}(\omega))|^2 \, d\mathbb{P}(\omega) < \infty \right\},$$

with respect to the probability measure $f_{\mathbf{X}}(\mathbf{x})d\mathbf{x}$. In linear elasticity applications, the function

$$y(\mathbf{X}) := y(\mathbf{u}(\mathbf{z};\mathbf{X}), \boldsymbol{\sigma}(\mathbf{z};\mathbf{X})), \tag{11}$$

written here with a certain abuse of notation, typically stems from the solutions $\mathbf{u} : \mathcal{D}\times\Omega \to \mathbb{R}^d$ and $\boldsymbol{\sigma} : \mathcal{D}\times\Omega \to \mathbb{R}^{d(d+1)/2}$ of the parameterized stochastic PDE described by (3). A principal objective of solving the stochastic problem from linear elasticity, in particular, and from solid mechanics, in general, is to effectively estimate the relevant probabilistic characteristics of $y(\mathbf{X}) \in L^2(\Omega,\mathcal{F},\mathbb{P})$. The dimension N of a real-life stochastic problem often exceeds 10 and may even be in the realm of hundreds, where the output response function $y(\mathbf{X})$ is highly nonlinear with locally significant changes, including discontinuity and nonsmoothness, with respect to the random input $\mathbf{X}$. Therefore, probabilistic computations for complex mechanical systems in a high-dimensional stochastic domain $\mathbb{A}^N$ is an expensive initiative.

3.1. ANOVA dimensional decomposition

Denote by u a subset of the index set $\{1,\ldots,N\}$ with the complementary set $-u := \{1,\ldots,N\}\backslash u$ and cardinality $0 \le |u| \le N$. Let $\mathbf{X}_u = (X_{k_1},\ldots,X_{k_{|u|}})$, $u \ne \emptyset, 1 \le k_1 < \cdots < k_{|u|} \le N$, be a subvector of $\mathbf{X}$ with $\mathbf{X}_{-u} := \mathbf{X}_{\{1,\ldots,N\}\backslash u}$ defining its complementary subvector. Then, for a given $\emptyset \ne u \subseteq \{1,\ldots,N\}$, the marginal density function of $\mathbf{X}_u$, defined on $\mathbb{A}^u := \times_{k\in u}\mathbb{A}^{\{k\}} \subset \mathbb{R}^{|u|}$, is

$$f_{\mathbf{X}_u}(\mathbf{x}_u) := \int_{\mathbb{A}^{-u}} f_{\mathbf{X}}(\mathbf{x}) d\mathbf{x}_{-u} = \prod_{k\in u} f_{X_k}(x_k),$$

where the second equality forms due to statistical independence of the input random variables as per Assumption 1. Hence, it can be shown that, for any function $y \in L^2(\Omega,\mathcal{F},\mathbb{P})$, there exists a unique, finite, hierarchical expansion [21,45]

$$y(\mathbf{X}) = y_\emptyset + \sum_{\emptyset\ne u\subseteq\{1,\ldots,N\}} y_u(\mathbf{X}_u), \tag{12a}$$

$$y_{\emptyset} := \int_{\mathbb{A}^N} y(\mathbf{x}) f_{\mathbf{X}}(\mathbf{x}) d\mathbf{x}, \tag{12b}$$

$$y_u(\mathbf{X}_u) := \int_{\mathbb{A}^{-u}} y(\mathbf{X}_u, \mathbf{x}_{-u}) f_{\mathbf{X}_{-u}}(\mathbf{x}_{-u}) d\mathbf{x}_{-u} - \sum_{v \subset u} y_v(\mathbf{X}_v), \tag{12c}$$

referred to as ADD, where y_u is a $|u|$-variate component function describing a constant or an $|u|$-variate interaction of $\mathbf{X}_u = (X_{k_1}, \ldots, X_{k_{|u|}})$ on y when $|u| = 0$ or $|u| > 0$. Here, $(\mathbf{X}_u, \mathbf{x}_{-u})$ denotes an N-dimensional vector whose kth component is X_k if $k \in u$ and x_k if $k \notin u$. The summation in (12a) comprises $2^N - 1$ terms with each term depending on a group of variables indexed by a particular subset of $\{1, \ldots, N\}$.

The decomposition presented in (12a)–(12c) has two notable properties [21]:

(1) Any non-constant component function $y_u(\mathbf{X}_u)$ has a *zero* mean, that is,

$$\mathbb{E}[y_u(\mathbf{X}_u)] = 0, \ \emptyset \neq u \in \{1, \ldots, N\}. \tag{13}$$

(2) Any two distinct component functions $y_u(\mathbf{X}_u)$ and $y_v(\mathbf{X}_v)$ are mutually orthogonal, that is,

$$\mathbb{E}[y_u(\mathbf{X}_u) y_v(\mathbf{X}_v)] = 0, \ u, v \in \{1, \ldots, N\}, \ u \neq v. \tag{14}$$

Readers interested in further details of ADD are directed to prior works [21,45].

It is elementary to show that all ADD component functions of $y(\mathbf{X})$ are members of respective subspaces of $L^2(\Omega, \mathcal{F}, \mathbb{P})$. Unfortunately, the subspaces are infinite-dimensional. Therefore, a further discretization or refinement is necessary. In contrast to the past works on polynomial refinements, a new spline adaptation of the subspaces, spanning measure-consistent orthonormal B-splines, is proposed.

3.2. Measure-consistent orthonormal B-splines

For the coordinate direction k, $k = 1, \ldots, N$, define a positive integer $n_k \in \mathbb{N}$ and a non-negative integer $p_k \in \mathbb{N}_0$, representing the number of basis functions and degree, respectively. Then, a knot vector or sequence $\boldsymbol{\xi}_k := \{\zeta_{k,i_k}\}_{i_k=1}^{n_k+p_k+1}$ is defined on the interval $[a_k, b_k]$ by a non-decreasing sequence of real numbers, where ζ_{k,i_k} is the i_kth knot with $i_k = 1, 2, \ldots, n_k + p_k + 1$. For more details, refer to Appendix A and Chapter 2 of [30]. In this work, only open knot vectors are considered.

Denote by $B^k_{i_k,p_k,\boldsymbol{\xi}_k}(x_k)$ the i_kth univariate B-spline with degree p_k. Given the knot sequence $\boldsymbol{\xi}_k$ and zero-degree basis functions, all higher-order B-spline functions on $[a_k, b_k]$ are defined recursively, where $1 \leq k \leq N$, $1 \leq i_k \leq n_k$, and $1 \leq p_k < \infty$. See Appendix A for an explicit definition of $B^k_{i_k,p_k,\boldsymbol{\xi}_k}(x_k)$.

The B-splines are endowed with a number of desirable properties, which can generally deliver tremendous approximating power to numerical methods. More specifically, they are [30,46]: (1) non-negative; (2) locally supported on the interval $[\zeta_{k,i_k}, \zeta_{k,i_k+p_k+1})$ for all i_k; (3) linearly independent; (4) committed to partition of unity; and (5) pointwise C^∞-continuous everywhere except at the knots ζ_{k,i_k} of multiplicity m_{k,i_k}, where they are $C^{p_k - m_{k,i_k}}$-continuous, provided that $1 \leq m_{k,i_k} < p_k + 1$.

3.2.1. Univariate orthonormal B-splines

The aforementioned B-splines, although they form a basis, are not orthogonal. A linear transformation, originally proposed in the companion paper [40], is summarized here in three steps to generate their orthonormal version.

(1) Given a set of B-splines of degree p_k, create an auxiliary set by replacing the first element with 1. Arrange the elements of the set into an n_k-dimensional vector

$$\mathbf{P}_k(x_k) := (1, B^k_{2,p_k,\boldsymbol{\xi}_k}(x_k), \ldots, B^k_{n_k,p_k,\boldsymbol{\xi}_k}(x_k))^T$$

comprising the auxiliary B-splines. The auxiliary B-splines are also linearly independent [40].

(2) Construct an $n_k \times n_k$ spline moment matrix

$$\mathbf{G}_k := \mathbb{E}[\mathbf{P}_k(X_k)\mathbf{P}_k^T(X_k)].$$

The matrix $\mathbf{G}_k$ exists because X_k has finite moments up to order $2p_k$, as stated in Assumption 1. It is symmetric and positive-definite [40], ensuring the existence of a non-singular $n_k \times n_k$ whitening matrix $\mathbf{W}_k$ such that

$$\mathbf{W}_k^T \mathbf{W}_k = \mathbf{G}_k^{-1}.$$

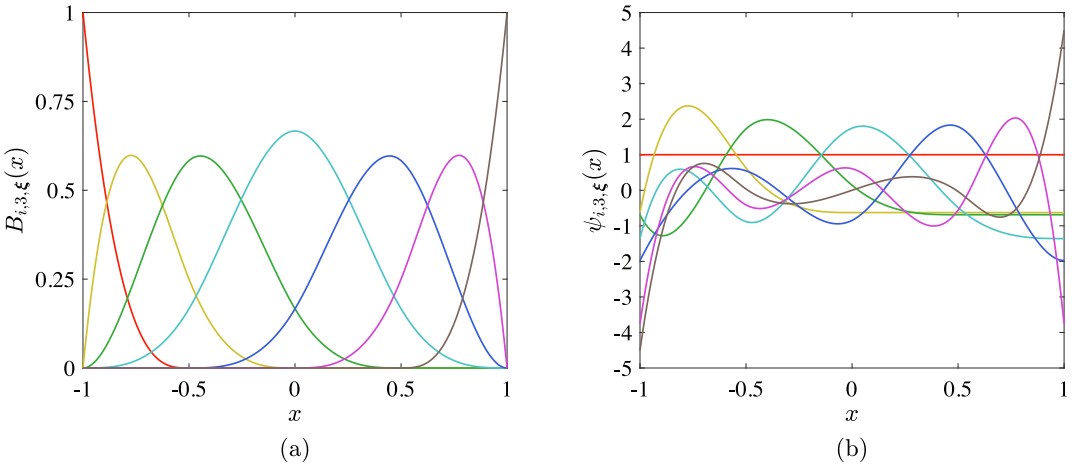

Fig. 1. A set of B-splines associated with the knot vector $\boldsymbol{\xi} = \{-1, -1, -1, -1, -0.5, 0, 0.5, 1, 1, 1, 1\}$ and order $p = 3$: (a) original B-splines, and (b) orthonormalized B-splines with respect to a uniform PDF on $[-1, 1]$.

(3) Apply a whitening transformation to create a vector of orthonormal B-splines

$$\boldsymbol{\psi}_k(x_k) = \mathbf{W}_k \mathbf{P}_k(x_k),$$

consisting of uncorrelated components $\psi^k_{i_k,p_k,\boldsymbol{\xi}_k}(x_k)$, $i_k = 1, \ldots, n_k,\ k = 1, \ldots, N$. However, the invertibility of $\mathbf{G}_k$ does not uniquely determine $\mathbf{W}_k$. Indeed, there are various options to choose $\mathbf{W}_k$ from, all satisfying the condition described in Step 2 [40]. One prominent choice is to invoke the Cholesky factorization: $\mathbf{G}_k = \mathbf{Q}_k \mathbf{Q}_k^T$, yielding

$$\mathbf{W}_k = \mathbf{Q}_k^{-1}.$$

Fig. 1 depicts a set of B-spline functions with the knot vector $\boldsymbol{\xi} = \{-1, -1, -1, -1, -0.5, 0, 0.5, 1, 1, 1, 1\}$ and order $p = 3$, before and after orthonormalization with respect to a uniform density function of a random variable X on the domain $[-1, 1]$. The original and orthonormal B-splines are plotted in Fig. 1(a) and Fig. 1(b), respectively. The whitening matrix is obtained from the Cholesky factorization. Note that after orthonormalization, the B-splines are neither non-negative nor locally supported. Having orthonormal basis functions, however, is a necessity before proceeding with spline refinement of ADD as ANOVA is constructed via orthogonal component functions. As discernible in Fig. 1(b), all non-constant functions have zero mean.

3.2.2. Multivariate orthonormal B-splines

Due to the product-type probability measure of random input variables, measure-consistent multivariate orthonormal B-splines in N variables are easily built from the N-dimensional tensor product of measure-consistent univariate B-splines. However, forming such a tensor product in a high-dimensional setting is not recommended. Instead, the authors advocate constructing a series of tensor products in a dimensionwise manner.

For a subset $\emptyset \neq u = \{k_1, \ldots, k_{|u|}\} \subseteq \{1, \ldots, N\}$, let $\mathbf{X}_u := (X_{k_1}, \ldots, X_{k_{|u|}})^T$, defined on the abstract probability space $(\Omega^u, \mathcal{F}^u, \mathbb{P}^u)$, where Ω^u is the sample space of $\mathbf{X}_u$, $\mathcal{F}^u$ is a σ-algebra on Ω^u, and $\mathbb{P}^u$ is a probability measure. Define three multi-indices $\mathbf{i}_u := (i_{k_1}, \ldots, i_{k_{|u|}}) \in \mathbb{N}_0^{|u|}$, $\mathbf{n}_u := (n_{k_1}, \ldots, n_{k_{|u|}}) \in \mathbb{N}_0^{|u|}$, and $\mathbf{p}_u := (p_{k_1}, \ldots, p_{k_{|u|}}) \in \mathbb{N}_0^{|u|}$, representing the knot indices, numbers of basis functions, and degrees of splines, respectively, in all $|u|$ coordinate directions. Associated with $\mathbf{i}_u$, define an index set

$$\mathcal{I}_{u,\mathbf{n}_u} := \left\{\mathbf{i}_u = (i_{k_1}, \ldots, i_{k_{|u|}}) : 1 \leq i_{k_l} \leq n_{k_l},\ l = 1, \ldots, |u|\right\} \subset \mathbb{N}^{|u|}$$

with cardinality

$$|\mathcal{I}_{u,\mathbf{n}_u}| = \prod_{k \in u} n_k.$$

For the coordinate direction k_l, define by

$$I_{k_l} = r_{k_l} - 1,$$

the number of subintervals corresponding to the knot vector $\boldsymbol{\xi}_{k_l}$ with r_{k_l} distinct knots. Then the partition, defined by the knot sequences $\boldsymbol{\xi}_{k_1}, \ldots, \boldsymbol{\xi}_{k_{|u|}}$, decomposes the $|u|$-dimensional rectangle $\mathbb{A}^u := \times_{k\in u}[a_k, b_k]$ into smaller rectangles

$$\mathbb{A}^u_{\mathbf{i}_u} = \left\{\mathbf{x}_u = (x_{k_1}, \ldots, x_{k_{|u|}}) : \zeta_{k_l,i_{k_l}} \le x_{k_l} < \zeta_{k_l,i_{k_l}+1},\ l = 1, \ldots, |u|\right\},$$
$$\mathbf{i}_u \in \left\{\mathbf{i}_u = (i_{k_1}, \ldots, i_{k_{|u|}}) : 1 \le i_{k_l} \le I_{k_l},\ l = 1, \ldots, |u|\right\} \subseteq \mathcal{I}_{u,\mathbf{n}_u},$$

where $\zeta_{k_l,i_{k_l}}$ is the i_{k_l}th distinct knot in the coordinate direction k_l. A mesh is defined by the partition of $\mathbb{A}^u$ into rectangular elements $\mathbb{A}^u_{\mathbf{i}_u}$, $\mathbf{i}_u \in \mathcal{I}_{u,\mathbf{n}_u}$. Define the largest element size in each coordinate direction $k \in u$ by

$$h_{u,k_l} := \max_{1\le l\le I_{k_l}} \left(\zeta_{k_l,l+1} - \zeta_{k_l,l}\right),\ l = 1, \ldots, |u|.$$

Then, given the knot sequences $\boldsymbol{\Xi}_u = \{\boldsymbol{\xi}_{k_1}, \ldots, \boldsymbol{\xi}_{k_{|u|}}\}$,

$$\mathbf{h}_u := (h_{u,k_1}, \ldots, h_{u,k_{|u|}}) \quad \text{and} \quad h_u := \max_{1\le l\le |u|} h_{u,k_l}$$

define a vector of the largest element sizes in all $|u|$ coordinates and the global mesh size, respectively, for the domain $\mathbb{A}^u$. Consequently, for $\emptyset \ne u = \{k_1, \ldots, k_{|u|}\} \subseteq \{1, \ldots, N\}$, with $\mathbf{p}_u = (p_{k_1}, \ldots, p_{k_{|u|}}) \in \mathbb{N}_0^{|u|}$ and $\boldsymbol{\Xi}_u = \{\boldsymbol{\xi}_{k_1}, \ldots, \boldsymbol{\xi}_{k_{|u|}}\}$ in mind, the multivariate B-splines in $\mathbf{x}_u = (x_{k_1}, \ldots, x_{k_{|u|}})$ consistent with the probability measure $f_{\mathbf{X}_u}(\mathbf{x}_u)d\mathbf{x}_u$ are

$$\Psi^u_{\mathbf{i}_u,\mathbf{p}_u,\boldsymbol{\Xi}_u}(\mathbf{x}_u) = \prod_{k\in u} \psi^k_{i_k,p_k,\boldsymbol{\xi}_k}(x_k) = \prod_{l=1}^{|u|} \psi^k_{i_{k_l},p_{k_l},\boldsymbol{\xi}_{k_l}}(x_{k_l}), \quad \mathbf{i}_u = (i_{k_1}, \ldots, i_{k_{|u|}}) \in \mathcal{I}_{u,\mathbf{n}_u}. \tag{15}$$

When the input random variables $X_1, \ldots, X_N$, instead of real variables $x_1, \ldots, x_N$, are inserted in the argument, the multivariate splines $\Psi^u_{\mathbf{i}_u,\mathbf{p}_u,\boldsymbol{\Xi}_u}(\mathbf{X}_u)$, $\emptyset \ne u \subseteq \{1, \ldots, N\}$, $\mathbf{i}_u \in \mathcal{I}_{u,\mathbf{n}_u}$, become functions of random input variables. To describe their second-moment properties succinctly, limit the index i_{k_l}, $l = 1, \ldots, |u|$, associated with the k_lth variable x_{k_l}, to run from 2 to n_{k_l}. The exclusion of $i_{k_l} = 1$ essentially removes the first constant element of $\boldsymbol{\psi}_k(X_k)$. Hence, define a reduced index set

$$\bar{\mathcal{I}}_{u,\mathbf{n}_u} := \left\{\mathbf{i}_u = (i_{k_1}, \ldots, i_{k_{|u|}}) : 2 \le i_{k_l} \le n_{k_l},\ l = 1, \ldots, |u|\right\} \subset (\mathbb{N} \setminus \{1\})^{|u|},$$

which has cardinality

$$|\bar{\mathcal{I}}_{u,\mathbf{n}_u}| := \prod_{k\in u}(n_k - 1). \tag{16}$$

Then, for $\emptyset \ne u, v \subseteq \{1, \ldots, N\}$, $\mathbf{i}_u \in \bar{\mathcal{I}}_{u,\mathbf{n}_u}$, and $\mathbf{j}_v \in \bar{\mathcal{I}}_{v,\mathbf{n}_v}$, the first- and second-order moments of multivariate orthonormal B-splines are [40]

$$\mathbb{E}\left[\Psi^u_{\mathbf{i}_u,\mathbf{p}_u,\boldsymbol{\Xi}_u}(\mathbf{X}_u)\right] = 0 \tag{17}$$

and

$$\mathbb{E}\left[\Psi^u_{\mathbf{i}_u,\mathbf{p}_u,\boldsymbol{\Xi}_u}(\mathbf{X}_u)\Psi^v_{\mathbf{j}_v,\mathbf{p}_v,\boldsymbol{\Xi}_v}(\mathbf{X}_v)\right] = \begin{cases} 1, & u = v \text{ and } \mathbf{i}_u = \mathbf{j}_v, \\ 0, & \text{otherwise}, \end{cases} \tag{18}$$

respectively. The orthonormal B-spline functions, defined in (15), are crucial ingredients of the proposed SDD method.

3.3. Fourier spline expansion

Consider any nonconstant component function of ADD defined in (12c). From the second-moment properties in (13) and (14), $y_u(\mathbf{X}_u)$ belongs to the Hilbert space

$$\mathcal{S}_u := \left\{y_u(\mathbf{X}_u) \in L^2(\Omega^u, \mathcal{F}^u, \mathbb{P}^u) : \mathbb{E}\left[y_u(\mathbf{X}_u)y_v(\mathbf{X}_v)\right] = 0 \text{ if } u \ne v, v \subseteq \{1, \ldots, N\}\right\}.$$

Denote by $\{\Psi^u_{\mathbf{i}_u,\mathbf{p}_u,\boldsymbol{\Xi}_u}(\mathbf{X}_u) : \mathbf{i}_u \in \bar{\mathcal{I}}_{u,\mathbf{n}_u}\}$ a set of measure-consistent multivariate orthonormal B-splines in $\mathbf{X}_u$. The size of the set is $|\bar{\mathcal{I}}_{u,\mathbf{n}_u}|$, as defined in (16). Therefore, it is controlled by the number of basis functions n_{k_l}, which, in turn, is determined from the length of the knot sequence $\boldsymbol{\xi}_{k_l}$ and order p_{k_l}. Clearly, the longer the sequence $\boldsymbol{\xi}_{k_l}$, the larger the n_{k_l} and, hence, the size of the set. For a refinement process with fixed $\mathbf{p}_u$, consider increasing the length of $\boldsymbol{\xi}_{k_l}$ or n_{k_l} in all $|u|$ coordinate directions, where the largest element size h_{u,k_l} is monotonically reduced. The result is an increasing family of the sets of such basis functions. In the limit, when $n_{k_l} \to \infty$, $k_l = 1, \ldots, |u|$, denote by $\boldsymbol{\xi}_{k_l,\infty}$ and $\boldsymbol{\Xi}_{u,\infty} = (\boldsymbol{\xi}_{1,\infty}, \ldots, \boldsymbol{\xi}_{|u|,\infty})$ the associated knot sequence in the k_lth coordinate direction and the set of such $|u|$ knot sequences, respectively. Then there exists an infinite number of basis functions with the associated index set

$$\bar{\mathcal{I}}_{u,\infty} := \left\{\mathbf{i}_u = (i_{k_1}, \ldots, i_{k_{|u|}}) : 2 \le i_{k_l} < \infty,\ l = 1, \ldots, |u|\right\},$$

representing the infinite counterpart of $\bar{\mathcal{I}}_{u,\mathbf{n}_u}$. In consequence, the infinite set of multivariate B-splines $\{\Psi^u_{\mathbf{i}_u,\mathbf{p}_u,\boldsymbol{\Xi}_{u,\infty}}(\mathbf{X}_u) : \mathbf{i}_u \in \bar{\mathcal{I}}_{u,\infty}\}$ forms an orthonormal basis of $\mathcal{S}_u$, yielding

$$\mathcal{S}_u = \overline{\text{span}\{\Psi^u_{\mathbf{i}_u,\mathbf{p}_u,\boldsymbol{\Xi}_{u,\infty}}(\mathbf{X}_u) : \mathbf{i}_u \in \bar{\mathcal{I}}_{u,\infty}\}},$$

where the overline stands for set closure.

According to the standard Hilbert space theory, every $y_u(\mathbf{X}_u) \in \mathcal{S}_u$ can be expanded in terms of the aforementioned spanning set, resulting in

$$y_u(\mathbf{X}_u) \sim \sum_{\mathbf{i}_u \in \bar{\mathcal{I}}_{u,\infty}} C^u_{\mathbf{i}_u,\mathbf{p}_u,\boldsymbol{\Xi}_\infty} \Psi^u_{\mathbf{i}_u,\mathbf{p}_u,\boldsymbol{\Xi}_{u,\infty}}(\mathbf{X}_u), \tag{19}$$

where

$$C^u_{\mathbf{i}_u,\mathbf{p}_u,\boldsymbol{\Xi}_{u,\infty}} := \int_{\mathbb{A}^u} y_u(\mathbf{x}_u)\Psi^u_{\mathbf{i}_u,\mathbf{p}_u,\boldsymbol{\Xi}_{u,\infty}}(\mathbf{x}_u) f_{\mathbf{X}_u}(\mathbf{x}) d\mathbf{x}_u = \int_{\mathbb{A}^N} y(\mathbf{x})\Psi^u_{\mathbf{i}_u,\mathbf{p}_u,\boldsymbol{\Xi}_{u,\infty}}(\mathbf{x}_u) f_{\mathbf{X}}(\mathbf{x}) d\mathbf{x},\ \ \mathbf{i}_u \in \bar{\mathcal{I}}_{u,\infty},$$

are the expansion coefficients. Here, the integral in the second equality forms when (12c) is applied to the first integral. Finally, combine (12c) and (19) to obtain the Fourier spline expansion

$$y(\mathbf{X}) \sim y_\emptyset + \sum_{\emptyset \ne u \subseteq \{1,\ldots,N\}} \sum_{\mathbf{i}_u \in \bar{\mathcal{I}}_{u,\infty}} C^u_{\mathbf{i}_u,\mathbf{p}_u,\boldsymbol{\Xi}_{u,\infty}} \Psi^u_{\mathbf{i}_u,\mathbf{p}_u,\boldsymbol{\Xi}_{u,\infty}}(\mathbf{X}_u), \tag{20}$$

where the constant component function $y_\emptyset$ is already defined in (12b). The expansion in (20) behaves like a Fourier series and is referred to as SDD in this paper. According to (20), the SDD of any random variable $y(\mathbf{X}) \in L^2(\Omega, \mathcal{F}, \mathbb{P})$ is a dimensionwise orthogonal projection onto the spline space spanning the set of associated measure-consistent multivariate orthonormal B-splines.

The relationship between SDD in (20) and ADD in (12a)–(12c) is obvious, as the former is derived by exploiting the spline adaptation of the latter. In addition, because of the orthonormality of basis functions, as described in (17) and (18), SDD inherits all the desirable properties of ADD, including the second-moment properties of $y_u(\mathbf{X}_u)$ described in (13) and (14). The SDD formulation of (20) is valid for any random function $y(\mathbf{X})$ and is, therefore, not specific to linear elasticity problems.

3.4. Truncation of SDD

In a practical setting, all knot sequences are finite, and so is the number of basis functions. In this case, a truncated set $\{\Psi^u_{\mathbf{i}_u,\mathbf{p}_u,\boldsymbol{\Xi}_u}(\mathbf{X}_u) : \mathbf{i}_u \in \bar{\mathcal{I}}_{u,\mathbf{n}_u}\}$ is used to approximate $y(\mathbf{X})$, resulting in the SDD approximation

$$y_{\mathbf{p},\boldsymbol{\Xi}}(\mathbf{X}) := y_\emptyset + \sum_{\emptyset \ne u \subseteq \{1,\ldots,N\}} C^u_{\mathbf{i}_u,\mathbf{p}_u,\boldsymbol{\Xi}_u} \Psi^u_{\mathbf{i}_u,\mathbf{p}_u,\boldsymbol{\Xi}_u}(\mathbf{X}_u) \tag{21}$$

with the expansion coefficients

$$C^u_{\mathbf{i}_u,\mathbf{p}_u,\boldsymbol{\Xi}_u} := \int_{\mathbb{A}^N} y(\mathbf{x})\Psi^u_{\mathbf{i}_u,\mathbf{p}_u,\boldsymbol{\Xi}_u}(\mathbf{x}_u) f_{\mathbf{X}}(\mathbf{x}) d\mathbf{x}, \quad \mathbf{i}_u \in \bar{\mathcal{I}}_{u,\mathbf{n}_u}. \tag{22}$$

From (21) and (22), there are

$$L_{\mathbf{p},\boldsymbol{\Xi}} = 1 + \sum_{s=1}^{N} \binom{N}{s} \prod_{k=1}^{s} (n_k - 1) = \prod_{k=1}^{N} n_k \tag{23}$$

expansion coefficients. Therefore, the SDD approximation suffers from the curse of dimensionality if all terms of (21) are retained. However, due to the dimensional hierarchical structure, many higher-variate interaction terms of SDD contribute only a negligible amount to the function value and therefore can be safely ignored. A straightforward approach to achieving this feat entails keeping all orthonormal splines in at most $0 \le S \le N$ variables, thereby retaining the degrees of interaction among input variables less than or equal to S. The result is an S-variate SDD approximation

$$y_{S,\mathbf{p},\boldsymbol{\Xi}}(\mathbf{X}) := y_{\emptyset} + \sum_{\substack{\emptyset \neq u \subseteq \{1,\ldots,N\} \\ 1 \le |u| \le S}} \sum_{\mathbf{i}_u \in \mathcal{I}_{u,\mathbf{n}_u}} C^{u}_{\mathbf{i}_u,\mathbf{p}_u,\boldsymbol{\Xi}_u} \Psi^{u}_{\mathbf{i}_u,\mathbf{p}_u,\boldsymbol{\Xi}_u}(\mathbf{X}_u) \tag{24}$$

of $y(\mathbf{X})$, comprising

$$L_{S,\mathbf{p},\boldsymbol{\Xi}} = 1 + \sum_{s=1}^{S} \binom{N}{s} \prod_{k=1}^{s} (n_k - 1) \le \prod_{k=1}^{N} n_k = L_{\mathbf{p},\boldsymbol{\Xi}} \tag{25}$$

expansion coefficients, including $y_{\emptyset}$. When $S = 1$ or $S = 2$, the resulting SDD approximations are referred to as univariate and bivariate SDD approximations, respectively. In such cases, the functions $y_{1,\mathbf{p},\boldsymbol{\Xi}}(\mathbf{X})$ or $y_{2,\mathbf{p},\boldsymbol{\Xi}}(\mathbf{X})$ should not be viewed as first- and second-order approximations, nor do they limit the nonlinearity of $y(\mathbf{X})$. Depending on how the orders and knot vectors are chosen, arbitrarily high-order univariate and bivariate terms of $y(\mathbf{X})$, including discontinuity and nonsmoothness, could be lurking inside $y_{1,\mathbf{p},\boldsymbol{\Xi}}(\mathbf{X})$ or $y_{2,\mathbf{p},\boldsymbol{\Xi}}(\mathbf{X})$.

Furthermore, if $S \ll N$, as it is envisioned to hold in practical applications, the number of coefficients in the S-variate SDD approximation declines sharply, resulting in significant computational savings. As an example, set $N = 15$, $n_k = 5$, and $S = 1$ or 2. Then there are more than 3×10^{10} coefficients in (23) versus 61 coefficients for $S = 1$ and 1741 coefficients for $S = 2$ in (25), demonstrating a substantial reduction in the computational effort while formulating univariate or bivariate SDD approximations. In general, the computational complexity of a truncated SDD ($S < N$) with respect to N is polynomial, as opposed to exponential, as in the case of PCE, thereby alleviating the curse of dimensionality to the extent possible.

The SDD approximations in (21) and (24) are both convergent to the correct limit in mean-square, in probability, and in distribution. Readers interested in formal proofs are referred to the companion paper [40].

3.5. Output statistics and other properties

The S-variate SDD approximation $y_{S,\mathbf{p},\boldsymbol{\Xi}}(\mathbf{X})$ can be viewed as an inexpensive surrogate of an expensive-to-calculate function $y(\mathbf{X})$. Therefore, pertinent statistical properties of $y(\mathbf{X})$, such as its first two moments, can be estimated from those of $y_{S,\mathbf{p},\boldsymbol{\Xi}}(\mathbf{X})$.

Applying the expectation operator on $y_{S,\mathbf{p},\boldsymbol{\Xi}}(\mathbf{X})$ in (24) and recognizing (17), its mean

$$\mathbb{E}\left[y_{S,\mathbf{p},\boldsymbol{\Xi}}(\mathbf{X})\right] = y_{\emptyset} = \mathbb{E}\left[y(\mathbf{X})\right] \tag{26}$$

is independent of S, $\mathbf{p}$, and $\boldsymbol{\Xi}$. More importantly, the SDD approximation always yields the exact mean, provided that the expansion coefficient $y_{\emptyset}$ is determined exactly.

Applying the expectation operator again, this time on $[y_{S,\mathbf{p},\boldsymbol{\Xi}}(\mathbf{X}) - y_{\emptyset}]^2$, and using (18) results in the variance

$$\operatorname{var}\left[y_{S,\mathbf{p},\boldsymbol{\Xi}}(\mathbf{X})\right] = \sum_{\substack{\emptyset \neq u \subseteq \{1,\ldots,N\} \\ 1 \le |u| \le S}} \sum_{\mathbf{i}_u \in \mathcal{I}_{u,\mathbf{n}_u}} C^{u^2}_{\mathbf{i}_u,\mathbf{p}_u,\boldsymbol{\Xi}_u} \le \operatorname{var}\left[y(\mathbf{X})\right] \tag{27}$$

of $y_{\mathbf{p},\boldsymbol{\Xi}}(\mathbf{X})$. Therefore, the second-moment statistics of an SDD approximation in (26) and (27) are determined based on a set of expansion coefficients. The formulae for the mean and variance of the SDD approximation are identical to those established for the PDD approximation, although the respective expansion coefficients involved are not. The fundamental reason for this similarity is rooted in the use of hierarchically ordered orthonormal basis function in both decomposition expressions.

Being convergent in probability and in distribution, the cumulative distribution function (CDF) and the PDF of $y(\mathbf{X})$, if it exists, can also be estimated economically by resampling $y_{S,\mathbf{p},\boldsymbol{\Xi}}(\mathbf{X})$. This will be illustrated in a numerical example.

3.6. Integration of SDD and IGA for linear elasticity problems

In linear elasticity applications, the random response function $y(\mathbf{X})$ defined in (11) depends on displacement $\mathbf{u}(\mathbf{z};\mathbf{X})$ and stress $\boldsymbol{\sigma}(\mathbf{z};\mathbf{X})$, which are obtained by solving the PDE in (3). The solution of the PDE, however, is generally not attainable in closed form. Having the IGA solver framework presented in Section 2.4.2, the approximated $\mathbf{u}^h(\mathbf{z};\mathbf{X})$ and approximated $\boldsymbol{\sigma}^h(\mathbf{z};\mathbf{X})$ are calculated instead. This is generally the case in reality when facing practical problems. Hence, for the problems involving linear elasticity and IGA, the random response function is redefined as

$$y(\mathbf{X}) \coloneqq y(\mathbf{u}^h(\mathbf{z};\mathbf{X});\boldsymbol{\sigma}^h(\mathbf{z};\mathbf{X})), \tag{28}$$

thereby integrating the proposed SDD method with the deterministic IGA solver. In simpler words, the random response function $y(\mathbf{X})$ under study is a function of approximate displacements and stresses rather than their exact counterparts. As a result, a source of error due to IGA discretization is already introduced to the numerical scheme, which is generally inevitable, but acceptable. The proposed stochastic method for linear elasticity applications shall thus be called SDD–IGA. But, for brevity, the term SDD will also be used. Note that starting with Section 4, SDD is a general term, which includes SDD–IGA, since the function evaluation process may be carried out through a non-intrusive IGA black box.

4. Dimension-reduction integration for expansion coefficients

The determination of the expansion coefficients of SDD, namely $y_\emptyset$ and $C^u_{\mathbf{i}_u,\mathbf{p}_u,\boldsymbol{\Xi}_u}$, involves various high-dimensional integrations. For an arbitrary function y and an arbitrary probability distribution of random input $\mathbf{X}$, an exact evaluation of these coefficients from definition alone is impossible. A natural instinct is to approximate the coefficients by numerical integration, for instance, by a general anisotropic $(Q_{k_1},\ldots,Q_{k_N})$-point, multivariate, tensor-product Gauss-type quadrature rule with $Q_{k_1},\ldots,Q_{k_N}\in\mathbb{N}$, yielding

$$y_\emptyset \simeq \underbrace{\sum_{j_{k_1}=1}^{Q_{k_1}}\cdots\sum_{j_{k_N}=1}^{Q_{k_N}}}_{N\text{ sums}} y(x_{k_1}^{(j_{k_1})},\ldots,x_{k_N}^{(j_{k_N})})\prod_{l=1}^{N} w_{k_l}^{(j_{k_l})}, \tag{29}$$

$$C^u_{\mathbf{i}_u,\mathbf{p}_u,\boldsymbol{\Xi}_u} \simeq \underbrace{\sum_{j_{k_1}=1}^{Q_{k_1}}\cdots\sum_{j_{k_N}=1}^{Q_{k_N}}}_{N\text{ sums}} y(x_{k_1}^{(j_{k_1})},\ldots,x_{k_N}^{(j_{k_N})})\prod_{l=1}^{|u|}\psi^{i_{k_l}}_{i_{k_l},p_{k_l},\boldsymbol{\xi}_{k_l}}(x_{k_l}^{(j_{k_l})})\prod_{l=1}^{N} w_{k_l}^{(j_{k_l})}, \tag{30}$$

where, for each $l=1,\ldots,N$, $x_{k_l}^{(j_{k_l})}$ and $w_{k_l}^{(j_{k_l})}$ are the integration points and matching weights, determined by the probability measure $f_{X_{k_l}}(x_{k_l})dx_{k_l}$. This is referred to as full integration in the paper. Recall that in linear elasticity applications, each value of function y in (29) and (30) is related to an IGA, as described in Section 3.6. Clearly, for a high-dimensional problem, say, with N exceeding 10, evaluating the N-dimensional sums in (29) or (30) is computationally formidable and likely prohibitive. Therefore, DRI is necessary to estimate these coefficients.

4.1. Dimension-reduction approximation

For a high-dimensional function $y(\mathbf{x})$, consider its referential dimensional decomposition (RDD) [21]

$$y(\mathbf{x}) = w_\emptyset + \sum_{\emptyset\neq u\subseteq\{1,\ldots,N\}} w_u(\mathbf{x}_u;\mathbf{c}), \tag{31}$$

where

$$w_\emptyset := y(\mathbf{c}),$$
$$w_u(\mathbf{x}_u; \mathbf{c}) := y(\mathbf{x}_u, \mathbf{c}_{-u}) - \sum_{v \subset u} w_v(\mathbf{x}_v; \mathbf{c}),$$

which is also known as cut-HDMR [47] and anchored decomposition [48]. Here, w_u is a $|u|$-variate RDD component function describing $|u|$-variate interaction of $\mathbf{X}_u$ on y, and $\mathbf{c} = (c_1, \ldots, c_N) \in \mathbb{A}^N$ is a chosen reference point. The second argument $\mathbf{c}$ appearing in w_u and w_v means that the RDD component functions also depend on the reference point, but y does not, as (31) is exact. Although RDD follows the same dimensional structure as ADD, the former does not feature the orthogonal property of the latter. This is the primary reason why ADD is favored over RDD for developing the SDD method. However, the RDD component functions are relatively easy to obtain as they only require function evaluations at the reference point, as opposed to the high-dimensional integration involved in ADD. As will be seen later, RDD is crucial for developing the DRI technique.

Given an integer $S \le R \le N$, the R-variate RDD approximation, say, $\hat{y}_R(\mathbf{x}; \mathbf{c})$ of $y(\mathbf{x})$, is obtained by truncating the right-hand side of (31), yielding

$$\hat{y}_R(\mathbf{X}; \mathbf{c}) = w_\emptyset + \sum_{\substack{\emptyset \ne u \subseteq \{1,\ldots,N\} \\ 1 \le |u| \le R}} w_u(\mathbf{x}_u; \mathbf{c}), \tag{32}$$

which also depends on the reference point, needing the second argument $\mathbf{c}$ in $\hat{y}_R$. From the work of Xu and Rahman [27], (32) has a direct form, so that RDD can also be written as

$$\hat{y}_R(\mathbf{x}; \mathbf{c}) = \sum_{r=0}^{R} (-1)^r \binom{N-R+r-1}{r} \sum_{\substack{\emptyset \ne v \subseteq \{1,\ldots,N\} \\ |v| = R-r}} y(\mathbf{x}_v, \mathbf{c}_{-v}) \tag{33}$$

in terms of the original function y explicitly. The direct form, under the names of dimension-reduction [49] and decomposition [50] methods, was employed for statistical moment and reliability analysis of mechanical systems, respectively. Although (33) was derived using the Taylor expansion, the function y is not restricted to be differentiable. Nonetheless, (32) and (33) follow the same dimensional structure, but the direct form of RDD is suitable for high-dimensional integration.

It is important to clarify that an optimal selection of the reference point $\mathbf{c}$ remains elusive. However, decent estimates of statistical moments and reliability were reported when the mean value of random input is selected as the reference point [27,48]. This work follows the same trend.

4.2. Reduced integration

In reference to (12b) and (22), replace the original function $y(\mathbf{X})$ in the integrands with the direct form of the R-variate RDD approximation $\hat{y}_R(\mathbf{X}; \mathbf{c})$ described in (33). As a result, the estimates $\hat{y}_\emptyset$ (say) and $\hat{C}^u_{\mathbf{i}_u, \mathbf{p}_u, \boldsymbol{\Xi}_u}$ (say) of the expansion coefficients $y_\emptyset$ and $C^u_{\mathbf{i}_u, \mathbf{p}_u, \boldsymbol{\Xi}_u}$ are

$$\hat{y}_\emptyset = \sum_{r=0}^{R} (-1)^r \binom{N-R+r-1}{r} \sum_{\substack{\emptyset \ne v \subseteq \{1,\ldots,N\} \\ |v| = R-r}} \int_{\mathbb{A}^v} y(\mathbf{x}_v, \mathbf{c}_{-v}) f_{\mathbf{X}_v}(\mathbf{x}_v) d\mathbf{x}_v \tag{34}$$

and

$$\hat{C}^u_{\mathbf{i}_u, \mathbf{p}_u, \boldsymbol{\Xi}_u} = \sum_{r=0}^{R} (-1)^r \binom{N-R+r-1}{r} \sum_{\substack{\emptyset \ne v \subseteq \{1,\ldots,N\} \\ |v| = R-r, u \subseteq v}} \int_{\mathbb{A}^v} y(\mathbf{x}_v, \mathbf{c}_{-v}) \Psi^u_{\mathbf{i}_u, \mathbf{p}_u, \boldsymbol{\Xi}_u}(\mathbf{x}_v) f_{\mathbf{X}_v}(\mathbf{x}_v) d\mathbf{x}_v, \tag{35}$$

respectively, requiring evaluation of multiple $|v|$-dimensional integrals. As $|v| = R - r$ and r varies from *zero* to R, at most R-dimensional integrals are involved. Therefore, the formulae (34) and (35) can be viewed to entail reduced integration, defending the appellation of DRI. Indeed, they are more efficient than calculating N-dimensional integrals, particularly when $R \ll N$. Hence, the computational effort in calculating the coefficients is significantly lowered by DRI, thereby deflating the curse of dimensionality. When $R = 1$ or 2, (34) and (35) involve one-, or at

most, two-dimensional integrals, respectively. When $R = N$, (34) and (35) transform to the original N-dimensional integrals from (12b) and (22), ensuring convergence of DRI.

It is important to emphasize that to obtain non-trivial estimates of the coefficients by DRI, R must be equal to or greater than the truncation parameter S. Furthermore, for computational expediency, the value of R should be as low as possible. Therefore, the selection of $R = S$ permits the most efficient calculation of the expansion coefficients for an S-variate SDD approximation.

For a general function y, numerical approximation is still required to approximate the $|v|$-dimensional integrals embedded in (34) and (35). If a $(Q_{k_1}, \ldots, Q_{k_{|v|}})$-point $|v|$-variate Gauss-type quadrature rule is used, then these integrals are approximated by

$$\int_{\mathbb{A}^v} y(\mathbf{x}_v, \mathbf{c}_{-v}) f_{\mathbf{X}_v}(\mathbf{x}_v) d\mathbf{x}_v \simeq \underbrace{\sum_{j_{k_1}=1}^{Q_{k_1}} \cdots \sum_{j_{k_{|v|}}=1}^{Q_{k_{|v|}}}}_{|v| \text{ sums}} y(x_{k_1}^{(j_{k_1})}, \ldots, x_{k_{|v|}}^{(j_{k_{|v|}})}) \prod_{l=1}^{|v|} w_{k_l}^{(j_{k_l})}$$

and

$$\begin{aligned} &\int_{\mathbb{A}^v} y(\mathbf{x}_v, \mathbf{c}_{-v}) \Psi^u_{\mathbf{i}_u, \mathbf{p}_u, \boldsymbol{\Xi}_u}(\mathbf{x}_v) f_{\mathbf{X}_v}(\mathbf{x}_v) d\mathbf{x}_v \\ \simeq &\underbrace{\sum_{j_{k_1}=1}^{Q_{k_1}} \cdots \sum_{j_{k_{|v|}}=1}^{Q_{k_{|v|}}}}_{|v| \text{ sums}} y(c_1, \ldots, c_{k_1-1}, x_{k_1}^{(j_{k_1})}, c_{k_1+1}, \ldots, c_{k_{|v|}-1}, x_{k_{|v|}}^{(j_{k_{|v|}})}, c_{k_{|v|}+1}, \ldots, c_N) \times \\ &\prod_{l=1}^{|u|} \psi^{i_{k_l}}_{i_{k_l}, p_{k_l}, \xi_{k_l}}\left(x_{k_l}^{(j_{k_l})}\right) \prod_{l=1}^{|v|} w_{k_l}^{(j_{k_l})}. \end{aligned}$$

The integration points and associated weights of DRI also depend on the probability distribution of $\mathbf{X}$ and are readily available, such as the Stieltjes procedure [49], to generate the measure-consistent Gauss quadrature formulae. The resultant estimation of $\hat{y}_\emptyset$ and $\hat{C}^u_{\mathbf{i}_u, \mathbf{p}_u, \boldsymbol{\Xi}_u}$, obtained using (34) and (35), is referred to as reduced integration in this paper.

4.3. Expanded version

While the compact notations enable a concise description of SDD, an expanded version using additional index notations should impart a better interpretation of the corresponding approximations. For instance, the S-variate SDD approximation can also be written as

$$\begin{aligned} y_{S,\mathbf{p},\boldsymbol{\Xi}}(\mathbf{X}) \;=\; & y_\emptyset + \sum_{k=1}^{N} \sum_{i_k=2}^{n_k} \alpha_{k i_k} \psi^k_{i_k, p_k, \xi_k}(X_k) + \\ & \sum_{k_1=1}^{N-1} \sum_{k_2=k_1+1}^{N} \sum_{i_{k_1}=2}^{n_{k_1}} \sum_{i_{k_2}=2}^{n_{k_2}} \beta_{k_1 k_2 i_{k_1} i_{k_2}} \psi^{k_1}_{i_{k_1}, p_{k_1}, \xi_{k_1}}(X_{k_1}) \psi^{k_2}_{i_{k_2}, p_{k_2}, \xi_{k_2}}(X_{k_2}) + \\ & \sum_{k_1=1}^{N-2} \sum_{k_2=k_1+1}^{N-1} \sum_{k_3=k_2+1}^{N} \sum_{i_{k_1}=2}^{n_{k_1}} \sum_{i_{k_2}=2}^{n_{k_2}} \sum_{i_{k_3}=2}^{n_{k_3}} \gamma_{k_1 k_2 k_3 i_{k_1} i_{k_2} i_{k_3}} \psi^{k_1}_{i_{k_1}, p_{k_1}, \xi_{k_1}}(X_{k_1}) \times \\ & \psi^{k_2}_{i_{k_2}, p_{k_2}, \xi_{k_2}}(X_{k_2}) \psi^{k_3}_{i_{k_3}, p_{k_3}, \xi_{k_3}}(X_{k_3}) + \cdots + \\ & \underbrace{\sum_{k_1=1}^{N-S+1} \cdots \sum_{k_S=k_{S-1}+1}^{N}}_{S \text{ sums}} \underbrace{\sum_{i_{k_1}=2}^{n_{k_1}} \cdots \sum_{i_{k_S}=2}^{n_{k_S}}}_{S \text{ sums}} C_{k_1 \ldots k_S i_{k_1} \ldots i_{k_S}} \prod_{s=1}^{S} \psi^{k_s}_{i_{k_s}, p_{k_s}, \xi_{k_s}}(X_{k_s}), \end{aligned}$$

where α_{ki_k}, $\beta_{k_1k_2i_{k_1}i_{k_2}}$, and $\gamma_{k_1k_2k_3i_{k_1}i_{k_2}i_{k_3}}$ are introduced to symbolize univariate, bivariate, and trivariate expansion coefficients, respectively. Moreover, the *zero*-variate and general S-variate expansion coefficients are defined as

$$y_{\emptyset} \coloneqq \int_{\mathbb{A}^N} y(x_1,\ldots,x_N)\prod_{k=1}^{N} f_{X_k}(x_k)dx_k$$

and

$$C_{k_1\ldots k_S i_{k_1}\ldots i_{k_S}} \coloneqq \int_{\mathbb{A}^N} y(x_1,\ldots,x_N)\prod_{s=1}^{S}\psi^{k_s}_{i_{k_s},p_{k_s},\xi_{k_s}}(x_{k_s})\prod_{k=1}^{N} f_{X_k}(x_k)dx_k,$$

respectively. Finally, the estimated expansion coefficients from DRI are

$$\hat{y}_{\emptyset} = \sum_{r=0}^{R}(-1)^r\binom{N-R+r-1}{r}\underbrace{\sum_{k_1=1}^{N-R+r+1}\cdots\sum_{k_{R-r}=k_{R-r-1}+1}^{N}}_{(R-r)\text{ sums}}$$
$$\int_{\mathbb{A}^{\{k_1,\ldots,k_{R-r}\}}} y(c_1,\ldots,c_{k_1-1},x_{k_1},c_{k_1+1},\ldots,c_{k_{R-r}-1},x_{k_{R-r}},c_{k_{R-r}+1},\ldots,c_N)\prod_{l=1}^{R-r} f_{X_{k_l}}(x_{k_l})dx_{k_l}$$

and

$$\hat{C}_{k_1\ldots k_S i_{k_1}\ldots i_{k_S}} = \sum_{r=0}^{R}(-1)^r\binom{N-R+r-1}{r}\underbrace{\sum_{k_1=1}^{N-R+r+1}\cdots\sum_{k_{R-r}=k_{R-r-1}+1}^{N}}_{(R-r)\text{ sums}}$$
$$\int_{\mathbb{A}^{\{k_1,\ldots,k_{R-r}\}}} y(c_1,\ldots,c_{k_1-1},x_{k_1},c_{k_1+1},\ldots,c_{k_{R-r}-1},x_{k_{R-r}},c_{k_{R-r}+1},\ldots,c_N)\times$$
$$\prod_{l=1}^{S}\psi^{k_l}_{i_{k_l},p_{k_l},\xi_{k_l}}(x_{k_l})\prod_{l=1}^{R-r} f_{X_{k_l}}(x_{k_l})dx_{k_l}.$$

These expanded versions are particularly useful in light of univariate ($S=1$), bivariate ($S=2$), and trivariate ($S=3$) approximations of SDD, to be illustrated in the numerical examples. Implementing the DRI, Appendix B provides examples of the expansion coefficients for the three specific cases of $S=1$, $S=2$, and $S=3$.

4.4. Computational effort

The S-variate SDD approximation $y_{S,\mathbf{p},\boldsymbol{\Xi}}(\mathbf{X})$ requires evaluations of $L_{S,\mathbf{p},\boldsymbol{\Xi}}$ expansion coefficients: $y_{\emptyset}$ and $C_{k_1\ldots k_S i_{k_1}\ldots i_{k_S}}$, $k_1=1,\ldots,N-s+1,\ \cdots,\ k_s=k_{s-1}+1,\ldots,N$, $i_{k_1}=2,\ldots,n_{k_1},\ \cdots,\ i_{k_s}=2,\ldots,n_{k_s}$, $s=1,\ldots,S$. Suppose these coefficients are to be estimated by the DRI technique with $S\le R\le N$, involving at most an R-dimensional tensor product of a $(Q_{k_1},\ldots,Q_{k_R})$-point univariate Gauss quadrature rule. Then the following deterministic responses from IGA or function evaluations are asked for:

(1) $y(\mathbf{c})$;
(2) $y(c_1,\ldots,c_{k_1-1},x_{k_1}^{(j_{k_1})},c_{k_1+1},\ldots,c_{k_r-1},x_{k_r}^{(j_{k_r})},c_{k_r+1},\ldots,c_N)$, $j_{k_1}=1,\ldots,Q_{k_1},\ \cdots,\ j_{k_r}=1,\ldots,Q_{k_r}$, $r=1,\ldots,R$, where the superscripts on variables indicate corresponding integration points.

However, since the B-splines are piecewise polynomials and not necessarily smooth functions on the entire domain $\mathbb{A}^{\{k_1,\ldots,k_{R-r}\}}$, a very large value of Q_{k_l}, $l=1,\ldots,R-r$, is required for accurate calculation of the integrals. A convenient alternative for numerical computation of the integrals involving piecewise polynomials is to break the domain of each integral into subintervals and then sum up their individual contributions.

Denote by q_{k_l} the number of integration points on each subinterval, and by $\mathbf{q}=(q_{k_1},\ldots,q_{k_l})$, the collection of such numbers for all k_l coordinate directions of the stochastic domain. Then, in the DRI framework, there are $Q_{k_l}=q_{k_l}I_{k_l}$ integration points in the coordinate direction k_l. Recall that I_{k_l} refers to the number of subintervals.

As a result, the total cost for calculating the expansion coefficients of the S-variate SDD approximation entails

$$1+\sum_{r=1}^{R}\underbrace{\sum_{k_1=1}^{N-r+1}\cdots\sum_{k_r=k_{r-1}+1}^{N}}_{r\text{ sums}}\prod_{l=1}^{r}(q_{k_l}I_{k_l}) \tag{36}$$

function evaluations. If I_{k_l} and q_{k_l} do not vary with k_l and are the same as I (say) and q (say), respectively, then the number of function evaluations becomes

$$1+\sum_{r=1}^{R}\underbrace{\sum_{k_1=1}^{N-r+1}\cdots\sum_{k_r=k_{r-1}+1}^{N}}_{r\text{ sums}}(qI)^r=\sum_{r=0}^{R}\binom{N}{R-r}(qI)^{R-r}. \tag{37}$$

For the latter case, consider the univariate, bivariate, and trivariate SDD approximations. Then the respective numbers of function evaluations using $R=S$ are as follows:

(1) Univariate approximation ($R=S=1$): $1+N(qI)$.
(2) Bivariate approximation ($R=S=2$): $1+N(qI)+N(N-1)(qI)^2/2$.
(3) Trivariate approximation ($R=S=3$): $1+N(qI)+N(N-1)(qI)^2/2+N(N-1)(N-2)(qI)^3/6$.

According to (34) or (35), the computational complexity of the SDD approximation is an Sth-order polynomial with respect to the number of random variables or integration points. This is possible because of the dimensional hierarchy of SDD.

Fig. 2 indicates a flowchart of the SDD–IGA method with the objective of constructing an S-variate approximation of the random response function $y(\mathbf{X})$ defined in (28). For reduced integration, DRI or any alternative method may be applied to efficiently estimate the expansion coefficients. However, while using the analytical formulae or even the regression methods, there is a need to run the deterministic IGA solver for a number of times, as discussed previously, to have samples of $y(\mathbf{X})$. This is done by the IGA solver illustrated in Fig. 2. The quality of the S-variate approximation, eventually, relies on the knot vectors $\boldsymbol{\Xi}$, B-splines orders $\mathbf{p}$, numbers of integration points on the subintervals $\mathbf{q}$, the truncation parameter S in (24), and the parameter R if implementing DRI. In agreement with Fig. 2, for a fixed IGA discretization, these input parameters may be controlled to obtain a desired accuracy.

On the other hand, coupling the same IGA solver described in Section 2.4.2 with PDD [35,51], a stochastic method is established, which shall be called PDD–IGA. However, for brevity in this paper, it will be referred to solely as PDD. In this case, since the PDD also engenders polynomial computational complexity, a relative comparison between the numbers of function evaluations by an S-variate SDD approximation in (36) or (37) and by an S-variate, mth-order PDD approximation [35,51] should be intriguing. For stochastic problems entailing smooth response functions, the computational cost of SDD is expected to be larger than that of PDD. This is because of the additional factor $I_{k_l}\geq 1$ or $I_k\geq 1$ originating from the subintervals, whereas no such factor exists or is needed due to the globally supported polynomial, smooth basis functions in PDD. In contrast, if the response function is discontinuous or nonsmooth, an impractically high order of PDD approximation will be required for satisfactory results, but will likely incur a cost that exceeds the computational budget. In the latter case, SDD becomes competitive and perhaps necessary to produce a desired solution with a reasonable cost. Nonetheless, if there are too many subintervals, the SDD method may also become expensive. This issue will be revisited when discussing numerical results.

5. Numerical examples

Four problems are put forward to illustrate the proposed SDD method for obtaining the second-moment statistics and probability distribution of various responses. Each example follows a particular objective: Example 1, not related to linear elasticity, makes a rigorous comparison between SDD and some of the favored UQ methods currently existing in the literature, while Examples 2 through 4 specifically entail linear elasticity problems. Example 2 compares the SDD and PDD methods, Example 3 evaluates the adequacy of the proposed DRI technique, and, finally, Example 4 handles a relatively complex geometry problem with a high stochastic dimension. The stress analyses were conducted using the standard IGA formulation discussed in Section 2 and Appendix A. The IGA

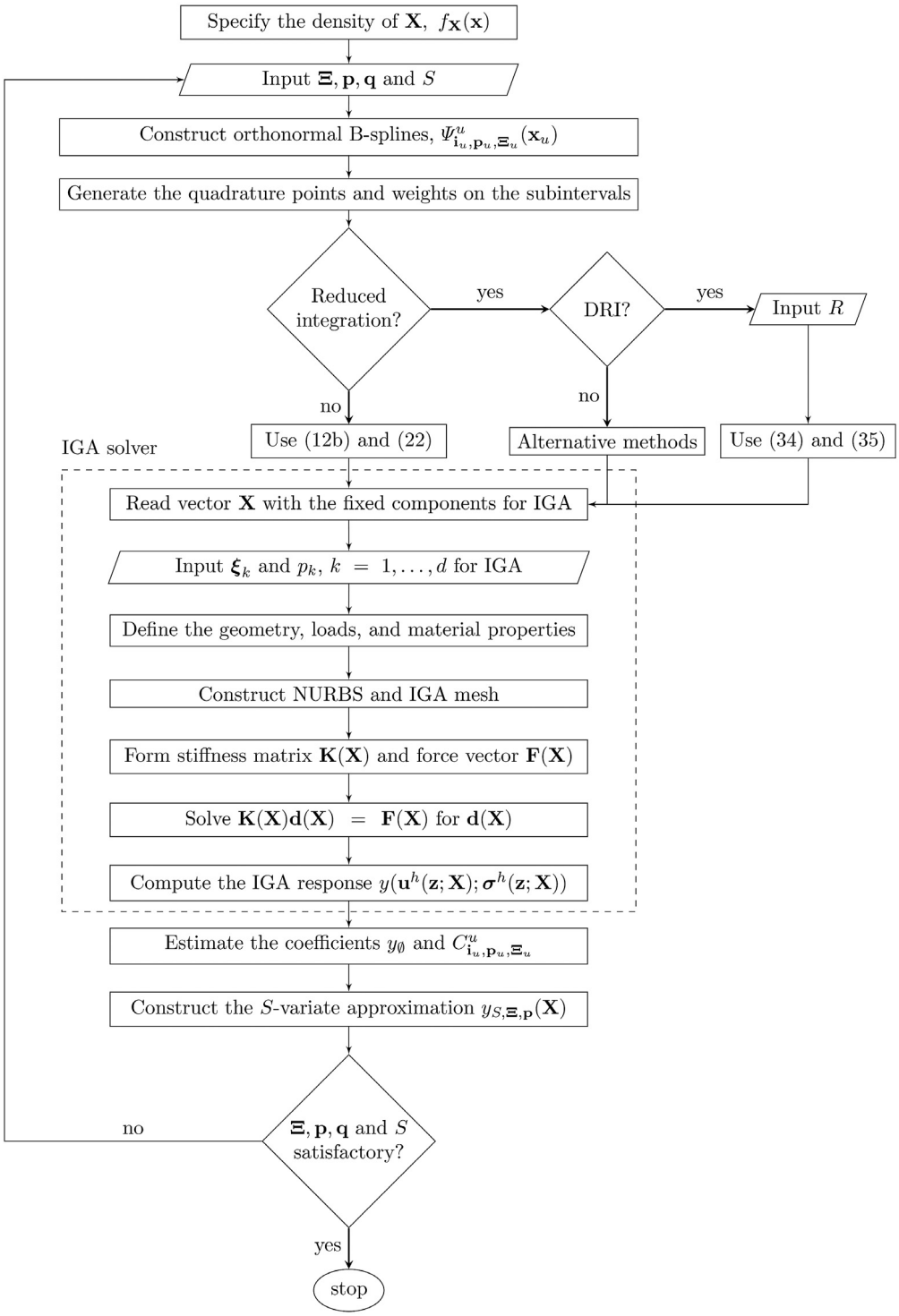

Fig. 2. A flowchart for the proposed SDD–IGA method.

discretization was fixed and deemed adequate, justifying no need for deterministic error analysis. In the stochastic domain, the degrees p and knot vector $\boldsymbol{\xi}$ used for SDD calculations were identical in all coordinate directions.

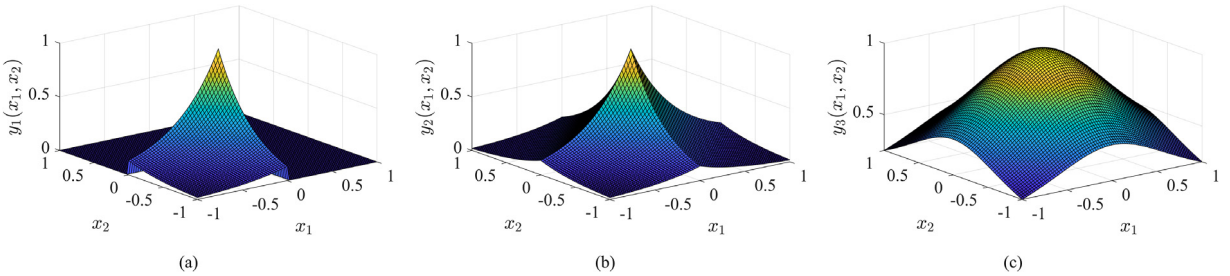

Fig. 3. Modified Genz functions in Example 1: (a) discontinuous, (b) continuous, and (c) product peak.

Hence, all subscripts k from p_k, $\boldsymbol{\xi}_k$, and I_k were dropped accordingly. For the DRI technique used in Examples 3 and 4, R was the same as the SDD truncation parameter S, and the mean input was selected as the reference point. A crude MCS was employed to provide the benchmark solutions in linear elasticity problems. The sample sizes for MCS were 10^8 in Example 2, 10^5 in Example 3, and 10^4 in Example 4.

5.1. Example 1: Modified Genz functions

For the first numerical example, consider three N-variate modified Genz functions [52]

$$y_1(\mathbf{X}) = \prod_{i=1}^{N} f_i(X_i) \qquad \text{(discontinuous)},$$

$$y_2(\mathbf{X}) = \exp(-2\sum_{i=1}^{N} |X_i|) \qquad \text{(continuous)},$$

$$y_3(\mathbf{X}) = \prod_{i=1}^{N} \frac{1}{1+X_i^2} \qquad \text{(product peak)},$$

where

$$f_i(X_i) = \begin{cases} 0, & \text{if } X_i > 0, \\ \exp(2X_i), & \text{otherwise.} \end{cases}$$

Here, X_i, $i = 1, \ldots, N$, are independent and identical random variables with uniform distribution over $[-1, 1]$. There is diversity in the functions' regularity, as illustrated in Fig. 3 for bivariate ($N = 2$) functions $y_1(X_1, X_2)$, $y_2(X_1, X_2)$, and $y_3(X_1, X_2)$. The objective is to study the second-moment statistical characteristics by various methods. Note that the Genz functions were introduced to test various integration techniques for mean calculation purposes [52]. Here, however, the variance is studied, which is even more challenging to compute. Hence, only powerful tools are expected to be able to accurately handle the variance. This is a remarkable opportunity to rigorously test the proposed SDD method before moving to linear elasticity applications.

The numerical investigations entailed two cases: bivariate ($N = 2$) and decavariate ($N = 10$) functions. For $N = 2$, the variances were calculated for $y_1(X_1, X_2)$, $y_2(X_1, X_2)$, and $y_3(X_1, X_2)$ exactly as $1.28743890 \times 10^{-2}$, $2.52956894 \times 10^{-2}$, and $3.25578478 \times 10^{-2}$, respectively. The variances were then also estimated by sparse grids with the Clenshaw–Curtis quadrature rule [53,54], tensor-product PCE [17,18], and the bivaraite, linear ($S = 2,\ p = 1$) and bivariate, quadratic ($S = 2,\ p = 2$) SDD methods. All PCE and SDD coefficients were calculated exactly as well. It is noteworthy that bivariate SDD is exact since $S = N = 2$. For $N = 10$, as exact computation of ten-dimensional integrals was not possible, the reference variances were calculated by crude MCS with 10^{10} samples as $7.41004195 \times 10^{-7}$, $7.68143090 \times 10^{-10}$, and $4.04864921 \times 10^{-3}$, for discontinuous, continuous, and product peak functions, respectively. In this case, PCE calculations were not feasible for the same reason, in addition to the curse of dimensionality. Moreover, the univariate, linear ($S = 1,\ p = 1$), bivariate, linear ($S = 2,\ p = 1$), and trivariate, linear ($S = 3,\ p = 1$) SDD coefficients were calculated by MCS with 3×10^7 samples. For all SDD approximations, in order to capture the discontinuity or nonsmoothness in discontinuous or continuous functions,

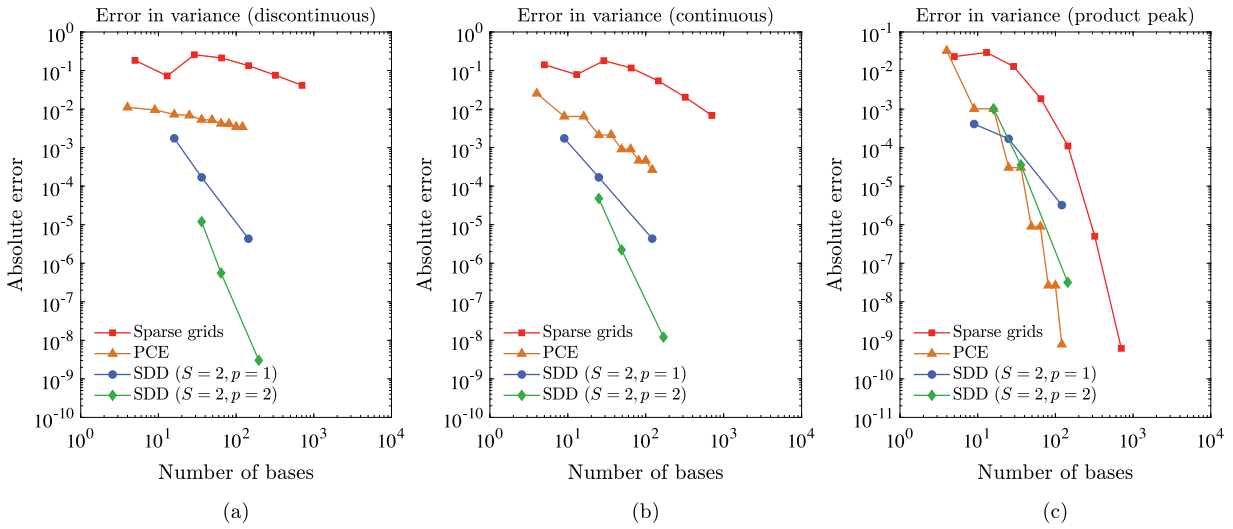

Fig. 4. Variance error analysis for bivariate ($N = 2$) modified Genz functions in Example 1: (a) discontinuous, (b) continuous, and (c) product peak.

respectively, the knots at $x_i = 0,\ i = 1, \ldots, N$ were repeated accordingly to harness the potential capabilities of SDD. Eventually, the errors were calculated versus the number of basis functions, which itself increased with the number of levels for sparse grids, the maximum polynomial order for PCE, and the number of subintervals for a given B-spline order in the case of SDD. For instance, for $N = 2$, the number of levels in sparse grids varied from one to seven, the PCE order increased from one to ten, and there were two, four, and ten subintervals in the SDD calculations. Note that the number of bases for the sparse grids method is equivalent to the number of integration points.

Fig. 4 depicts how the absolute errors in variance, calculated by various methods, decay for discontinuous, continuous, and product peak functions. According to Fig. 4(a) and (b), the sparse grids and PCE methods struggle to provide results as accurate as those obtained by SDD methods of order (p) only up to two. This is due to the discontinuity and nonsmoothness in the functions. As observed, PCE and sparse grids perform slightly better on the continuous function than the discontinuous one. Moreover, the convergence is steeper for quadratic SDD than linear SDD in both cases. For the error decay corresponding to the product peak function, as the original function is rather smooth, all methods do well. Hence, SDD may not be needed in this case. Furthermore, the basis functions of odd order do not contribute to PCE approximations, as the original function is even, as demonstrated in Fig. 3(c). Overall, numerical evidence reveals significant contribution of the proposed SDD method in terms of both efficiency and accuracy, while the rate of convergence is also markedly higher for functions with harsh regularities, as expected.

The absolute variance errors corresponding to decavariate ($N = 10$) functions are illustrated in Fig. 5. Here, the univariate, bivariate, and trivariate SDD methods are compared only with sparse grids as PCE, suffering from low efficiency, was ruled out. Obviously, for a given number of basis functions, the SDD methods are substantially more accurate than sparse grids. By comparing Figs. 4 and 5, it is clear that the larger the N, the more devastating the problem becomes for sparse grids. Furthermore, SDD provides more accurate results with the increase in S. The errors in univariate, bivariate, and trivariate SDD methods, however, all reach a plateau in Fig. 5(a) and (b). The reason is that for approximation of such functions, a higher level of interaction between variables (S) is needed. In other words, for $S = 10 = N$, the trends would have been monotonically decreasing, as previously observed for $S = N = 2$ in Fig. 4. Of course, in order to keep the number of coefficients as low as possible, $S > 3$ was deemed unnecessary in this example. According to Fig. 5(c), the sparse grids method is marginally better for the case of smooth function, but still is inferior to SDD in terms of accuracy. It must be emphasized that for $N = 10$, neither the reference variance, nor the SDD coefficients were exact. Hence, the reported errors are approximate. The bottom line is that the proposed method is able to elegantly deal with harsh functions in terms of regularity. This

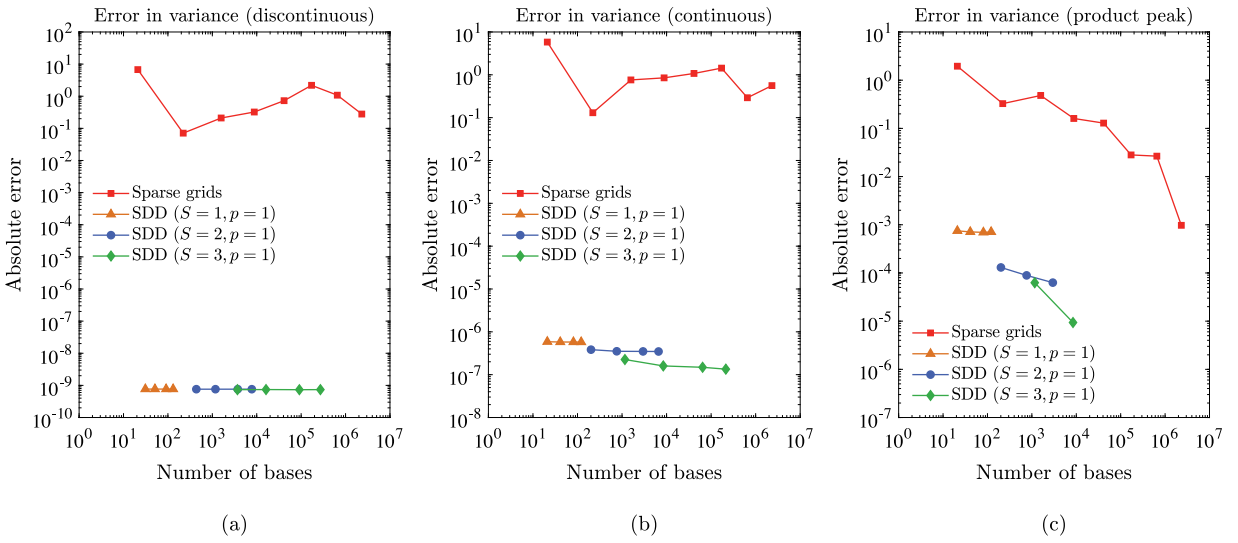

Fig. 5. Variance error analysis for decavariate ($N = 10$) modified Genz functions in Example 1: (a) discontinuous, (b) continuous, and (c) product peak.

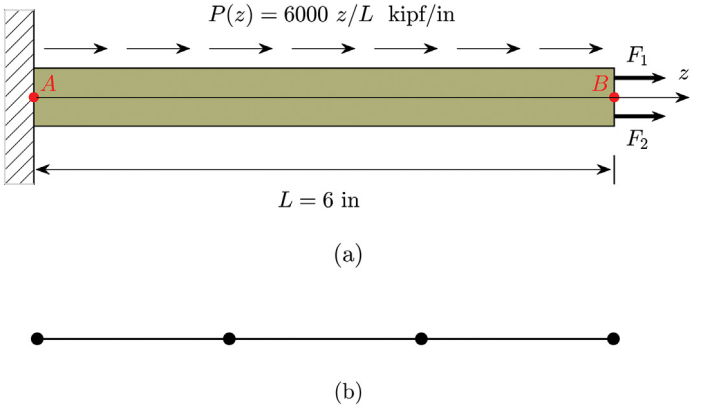

Fig. 6. A bar under uniaxial tension in Example 2: (a) problem schematic; (b) IGA mesh.

affordable method also surpasses PCE and sparse grids, when it comes to accuracy, while for high-dimensional problems, the dimension-wise structure of SDD yields accurate low-variate approximations. This will be further discussed for linear elasticity applications in Example 4.

5.2. Example 2: Bar under uniaxial loading

The second example illustrates a prismatic bar under a uniaxial loading along the z-axis in the physical space, as defined in Fig. 6(a). The bar is 6 inches long and is fixed at Point A ($z = 0$). Three external loads are applied to the bar: (1) a linearly distributed load $P(z) = 6z/L$ (kipf per inch); (2) a concentrated force F_1 (kipf) acting on the endpoint B at $z = L = 6$ inches, and (3) another concentrated force F_2 (kipf) applied to the endpoint B. The loads may be physically due to different sources. For instance, F_1 and F_2 may be applied by two separate pushing/pulling sources of energy, while $P(z)$ may be the effect of a magnetic field. A positive or negative value of F_1 or F_2 represents a tensile or compressive force, respectively.

While the cross section $A = 1$ in^2 and the length $L = 6$ in are both deterministic, the Young's modulus E and the forces F_1, F_2 are set as independent random variables with their statistical properties described in Table 1.

Table 1
Statistical properties of the random inputs in Example 2.

Random variable	Type	Bounds	Mean	Standard deviation	Units
F_1	Uniform	$[-20, 20]$	0	11.547	kipf
F_2	Uniform	$[-20, 20]$	0	11.547	kipf
E	Uniform	$[27 \times 10^6, 33 \times 10^6]$	30×10^6	1.732×10^6	lbf/in^2

The output response of interest, denoted by $\delta_B(\mathbf{X})$, is the absolute displacement of the endpoint B, which depends on the three-dimensional ($N = 3$) random input vector $\mathbf{X} = (F_1, F_2, E)$. The objective of this example is to compare the approximation quality of the SDD and PDD methods, while calculating the mean and standard deviation of δ_B.

The deterministic IGA involved three quadratic elements with the corresponding mesh shown in Fig. 6(b). Additional information about the control points, weights, and knot vector are provided in Table C.1 of Appendix C. In the stochastic domain of SDD, two B-spline orders, $p = 1$ and $p = 2$, representing linear and quadratic elements, respectively, were employed. Given p, four uniform knot vectors $\boldsymbol{\xi}$ in each of the three coordinate directions were chosen in such a way that the number of subintervals I varies as 2, 4, 6, and 8. The larger the I, the smaller the element size, and hence the finer the mesh in the stochastic domain $\mathbb{A}^3$. For numerical integration required for calculating the SDD expansion coefficients, a full integration involving an isotropic $(p + 1)$-point $(q = p + 1)$ Gauss quadrature rule was employed for each subinterval. For both SDD and PDD methods, three respective approximations resulting from univariate ($S = 1$), bivariate ($S = 2$), and trivariate ($S = 3$) truncations were used. The second-moment properties calculated by SDD were based on (26) and (27). The order m of PDD approximations was varied as 1, 2, 3, 5, 6, 8, 10, and 12. The second-moment properties by PDD were calculated using the reported formula from Gautschi [49]. A full integration involving an isotropic $(m + 1)$-point Gauss quadrature rule was used for estimating the PDD expansion coefficients. As the response function involves the absolute value of a displacement, a nonsmoothness exists in the original function, which is generally difficult to capture by globally supported, smooth basis functions. This explains the motivation for including PDD, to be contrasted with SDD. The relative errors committed by SDD and PDD approximations were assessed with respect to the crude MCS solution, which provided the following benchmark statistics: mean of $\delta_B(\mathbf{X})$ = 0.003356688 inch; standard deviation of $\delta_B(\mathbf{X})$ = 0.002370485 inch.

Fig. 7 illustrates the relative error in the mean values approximated by the PDD and SDD methods versus the corresponding number of requisite expansion coefficients. The number of expansion coefficients increases with the maximum polynomial order m for PDD and with the number of subintervals I and order p in the case of SDD. Based on Fig. 7, all methods are convergent and are able to accurately calculate the mean of the response. This is not a surprising finding as calculating the mean value is generally not difficult. However, as the mean is independent of the choice of the basis function, the more rigorous the numerical integration of (12b), the more precise the estimation of mean. The SDD method provides more accurate results than PDD since, for integration, the entire domain is broken into subintervals.

Moreover, the linear SDD method ($p = 1$) exhibits a more dominant convergence behavior than the quadratic SDD ($p = 2$) as the number of coefficients increases. The reason is that, with the refinement of the knot vectors, the knots tend to fall on the proximity of the nonsmoothness of the original function. Hence, the function is approximated better. In the case of the quadratic SDD ($p = 2$), however, as the knots are not repeated, the C^1-continuous approximate function is not able to represent nonsmoothness adequately. Hence, the linear SDD is superior to the quadratic SDD. Having said this, when the number of subintervals is low, the number of expansion coefficients is low, and the knots do not fall in a close neighborhood of nonsmoothness, and the quadratic SDD method provides better results than the linear SDD method as it is of higher order.

Fig. 8(a) through (c) demonstrate the convergence of the standard deviation of $\delta_B(\mathbf{X})$ estimated by the univariate, bivariate, and trivariate PDD and SDD methods. According to Fig. 8(a), all PDD and SDD methods reach a plateau, implying that the univariate approximation lacks accuracy. This is due to the bivariate interaction of F_1 and F_2 acting on δ_B, which is not captured by the univariate approximations. The errors get much lower for the bivariate and trivariate approximations, as depicted in Fig. 8(b) and 8(c), respectively. Furthermore, PDD methods struggle to estimate the standard deviation of δ_B as accurately as linear or quadratic SDD methods, although the order grows as large as 12. This is due to the nonsmoothness in the response function, which is impressively captured by SDD.

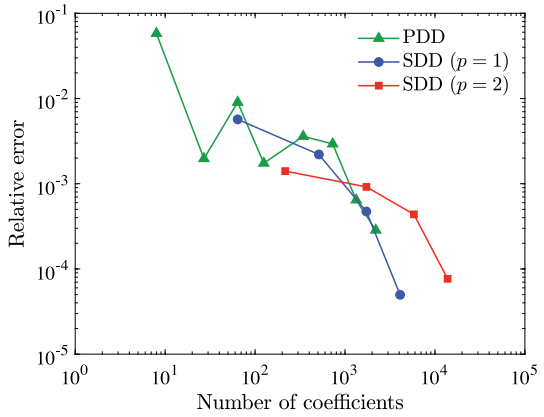

Fig. 7. Convergence of the mean to the benchmark value versus the number of expansion coefficients in Example 2.

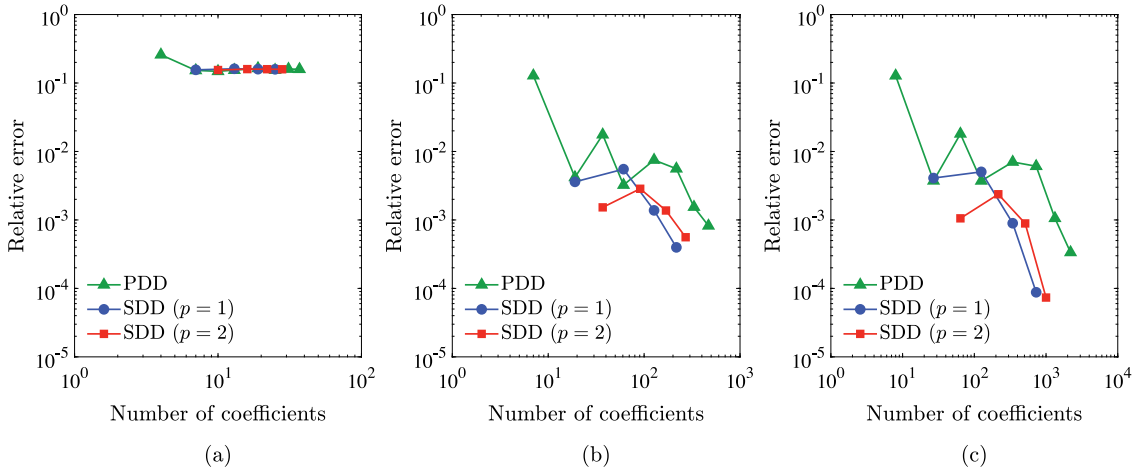

Fig. 8. Convergence of the standard deviation to the benchmark value versus the number of expansion coefficients in Example 2: (a) univariate ($S = 1$); (b) bivariate ($S = 2$); and (c) trivariate ($S = 3$) approximations.

Results improve with the increase in S where the trivariate approximation is the most accurate, as $S = N = 3$. Once more, linear SDD dominates quadratic SDD with the increase in the number of expansion coefficients for the same reason discussed previously. It is observed that the proposed SDD method is able to properly estimate the second-moment statistical properties of the response even with linear basis functions, whereas the PDD method with polynomials of maximum order up to 12 is unable to match in terms of accuracy.

5.3. Example 3: Plate with the hole problem

The main purpose of the third example is to evaluate the influence of the proposed DRI technique on the accuracy of the SDD method. Consider a square plate with a central circular hole. The plate is of length $2L$ units, and the hole is of radius a units, as illustrated in Fig. 9(a). The plate undergoes a uniaxial far-field tensile stress σ_∞ in the y-direction. The isotropic elastic properties of the material are completely defined by the Young's modulus E and the Poisson's ratio ν. The stochastic PDE associated with this problem entails five random variables ($N = 5$) with $\mathbf{X} = (L, a, E, \nu, \sigma_\infty)$. Their statistical properties are described in Table 2 in consistent units. The plate thickness is 1 unit. For simplicity, only a quarter of the plate was modeled due to the symmetry in the geometry and loading. The objective is to study the statistical properties of the displacements and stresses within the body due to the uncertainty in the input parameters described earlier.

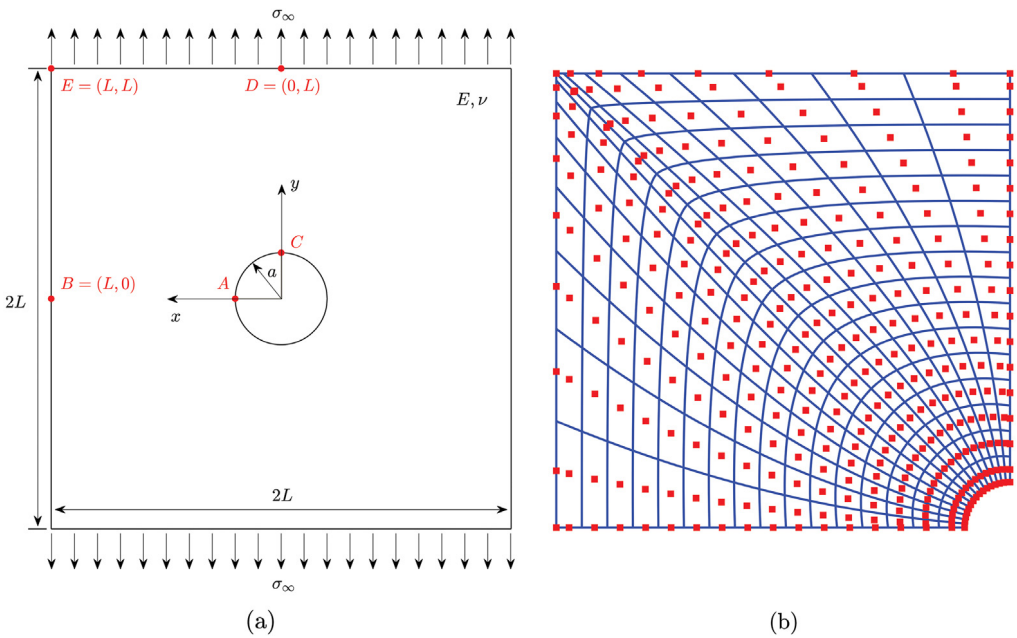

Fig. 9. A plate with a circular hole under uniaxial tension in the y-direction in Example 3: (a) problem schematic; (b) refined mesh employed in the analyses. The control points are illustrated by red closed squares.

Table 2
Statistical properties of the random inputs in Example 3.

Random variable	Type	Bounds	Mean	Standard deviation
L	Uniform	[9.5, 10.5]	10	0.2887
a	Uniform	[0.95, 1.05]	1	0.0289
E	Uniform	[0.8, 1.2]	1	0.1155
ν	Uniform	[3/10, 11/30]	1/3	0.0192
σ_∞	Lognormal	$(0, +\infty)$	1	0.15

Fig. 9(b) illustrates the IGA discretization on the exact single-patch geometry with the control points indicated by red closed squares. This mesh was generated by simple h-refinement on a base two-element mesh with knot vectors, control points, and weights defined in Tables C.2, C.3, and Fig. C.1 of Appendix C. The IGA mesh in Fig. 9(b) consists of a total of 256 quadratic elements. The corresponding control points for the refined mesh are too many to report. Two sets of solutions are provided, and their difference lies in the numerical calculation of the SDD coefficients: (1) full integration based on (12b) and (22); and (2) reduced integration entailing the DRI technique with additional Gauss quadrature approximations in (34) and (35). The SDD methods include bivariate, linear ($S = 2$, $p = 1$) and bivariate, quadratic ($S = 2$, $p = 2$) approximations, each with two subintervals ($I = 2$). The expansion coefficients were calculated with $(p + 1)$ Gauss points on each subinterval.

Tables 3 and 4 list the results for the mean and standard deviation computations, respectively, at various points of the plate, defined in Fig. 9(a). Here, u, σ, and τ symbolize displacement, normal stress, and shear stress, respectively. The displacements and stresses were calculated using (9) and (10), respectively, and the number of function evaluations or IGA for each method is noted in the parentheses. This number for reduced integration methods was computed using (37). It is observed that both means and standard deviations of the responses are accurately estimated by the SDD method when compared with the MCS solution. However, those calculations involving the DRI technique are tremendously more efficient as the numbers of IGA are much lower than those of the methods with full integration. The DRI has negligible impact on the accuracy, and the maximum error in mean predictions among all methods, also negligible at 0.18%, is obtained by the reduced integration approach with linear ($p = 1$) SDD.

Table 3
Mean of various responses at several points of the plate in consistent units in Example 3[a].

		Full integration[b]		Reduced integration[c]		
Point	Response	$p=1$ (1024)	$p=2$ (7776)	$p=1$ (181)	$p=2$ (391)	MCS (100,000)
	u_x	−1.071	−1.072	−1.071	−1.072	−1.072
A	σ_y	3.182	3.185	3.182	3.185	3.187
	τ_{xy}	−0.003808	−0.003812	−0.003808	−0.003812	−0.003813
B	u_x	−3.626	−3.630	−3.626	−3.630	−3.629
	σ_y	0.9746	0.9756	0.9746	0.9756	0.9760
	u_y	3.112	3.115	3.112	3.115	3.114
C	σ_x	−1.117	−1.118	−1.117	−1.118	−1.119
	τ_{xy}	0.001521	0.001523	0.001521	0.001523	0.001523
D	u_y	10.567	10.577	10.567	10.577	10.573
	σ_y	1.007	1.008	1.007	1.008	1.008
	u_x	−3.150	−3.153	−3.150	−3.153	−3.152
E	u_y	9.850	9.860	9.850	9.860	9.856
	σ_y	0.9987	0.9997	0.9987	0.9997	1.000

[a]The numbers of function evaluations are reported in parentheses.
[b]N-dimensional integrals are computed.
[c]The DRI technique is applied.

Table 4
Standard deviation of various responses at several points of the plate in consistent units in Example 3[a].

		Full integration[b]		Reduced integration[c]		
Point	Response	$p=1$ (1024)	$p=2$ (7776)	$p=1$ (181)	$p=2$ (391)	MCS (100,000)
	u_x	0.1945	0.2009	0.1953	0.2018	0.2081
A	σ_y	0.4281	0.4527	0.4280	0.4527	0.4802
	τ_{xy}	0.0005520	0.0005795	0.0005525	0.0005802	0.0006102
B	u_x	0.6816	0.7026	0.6849	0.7063	0.7254
	σ_y	0.1311	0.1386	0.1310	0.1386	0.1471
	u_y	0.5635	0.5821	0.5658	0.5847	0.6029
C	σ_x	0.1506	0.1592	0.1505	0.1592	0.1688
	τ_{xy}	0.0002101	0.0002216	0.0002103	0.0002218	0.0002345
D	u_y	1.906	1.969	1.913	1.978	2.038
	σ_y	0.1354	0.1432	0.1354	0.1432	0.1519
	u_x	0.6039	0.6218	0.6071	0.6254	0.6413
E	u_y	1.781	1.840	1.788	1.848	1.904
	σ_y	0.1343	0.1420	0.1343	0.1420	0.1507

[a]The numbers of function evaluations are reported in parentheses.
[b]N-dimensional integrals are computed.
[c]The DRI technique is applied.

On the other hand, there is a slight degradation in the accuracy of the values of standard deviation (Table 4) with or without the implementation of DRI. The maximum errors by full integration with $p=1$ and $p=2$ are 10.88% and 5.78%, respectively, compared to 10.94% and 5.78% by reduced integration. As a result, the DRI does not impose a significant impact on the accuracy of the standard deviation values either, while the number of function evaluations drops drastically from 1024 to 181 and from 7776 to 391 for the linear and quadratic SDD methods, respectively. Furthermore, all results generally improve with the increase in order p from 1 to 2.

Figs. 10 and 11 display the contour plots of the mean and standard deviation of displacement u_y, normal stress σ_y, and absolute value of shear stress $|\tau_{xy}|$ computed by crude MCS and bivariate, quadratic SDD approximation

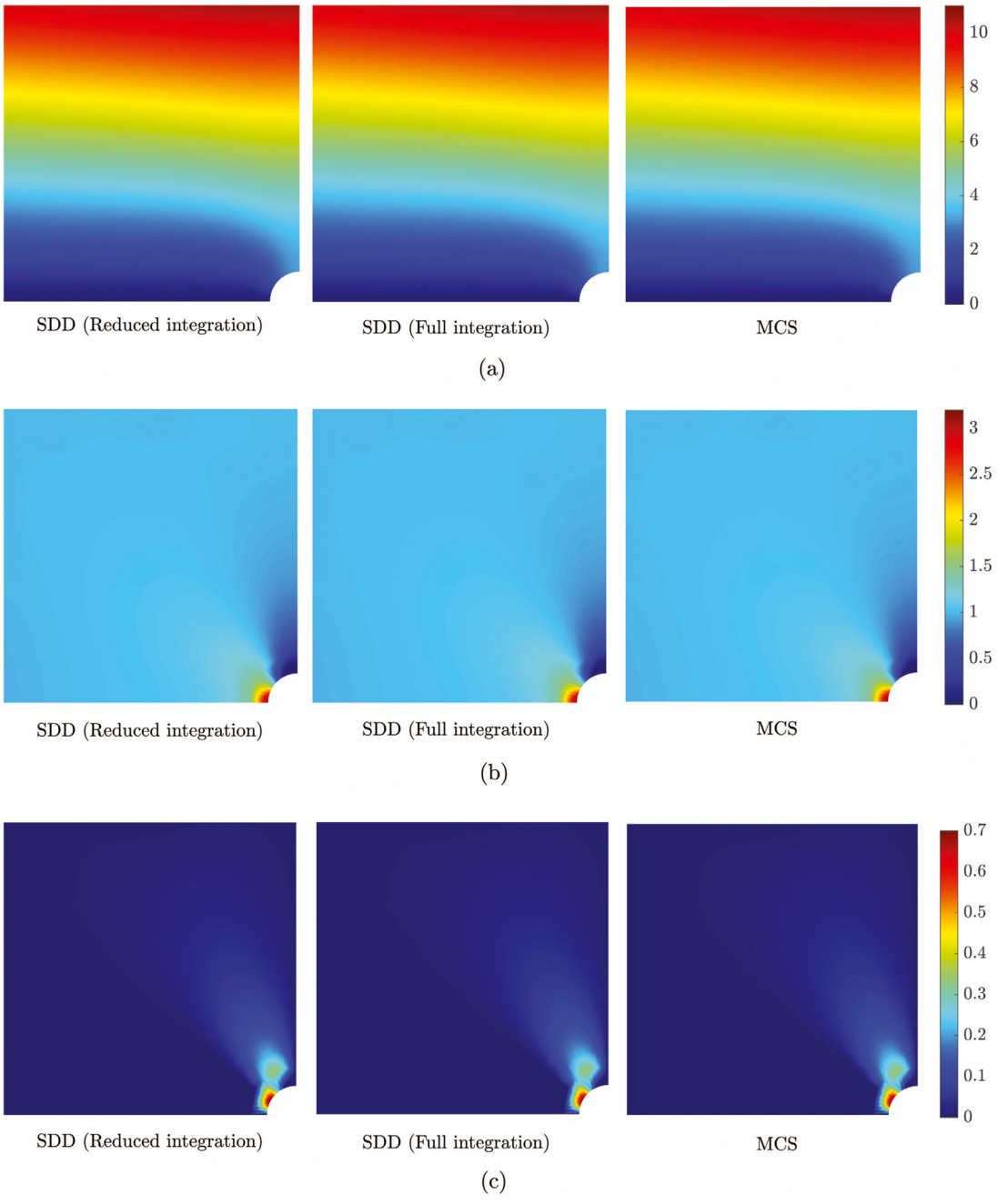

Fig. 10. Contour plots for the mean of (a) u_y, (b) σ_y, and (c) $|\tau_{xy}|$ obtained by SDD with reduced integration by DRI (left), SDD with full integration (middle), and MCS (right) in consistent units in Example 3.

with two subintervals ($S = 2$, $p = 2$, $I = 2$). Again, the purpose is to evaluate the accuracy of the results obtained from full integration and reduced integration (DRI), but this time over the whole physical domain. In agreement with previous statements, any difference in the contour plots by SDD and MCS is indiscernible to the naked eye. The increase in the order yields an increase in the number of basis functions and, by extension, the number of expansion coefficients, boosting the total number of IGA required by SDD. As a result, the larger the order and/or

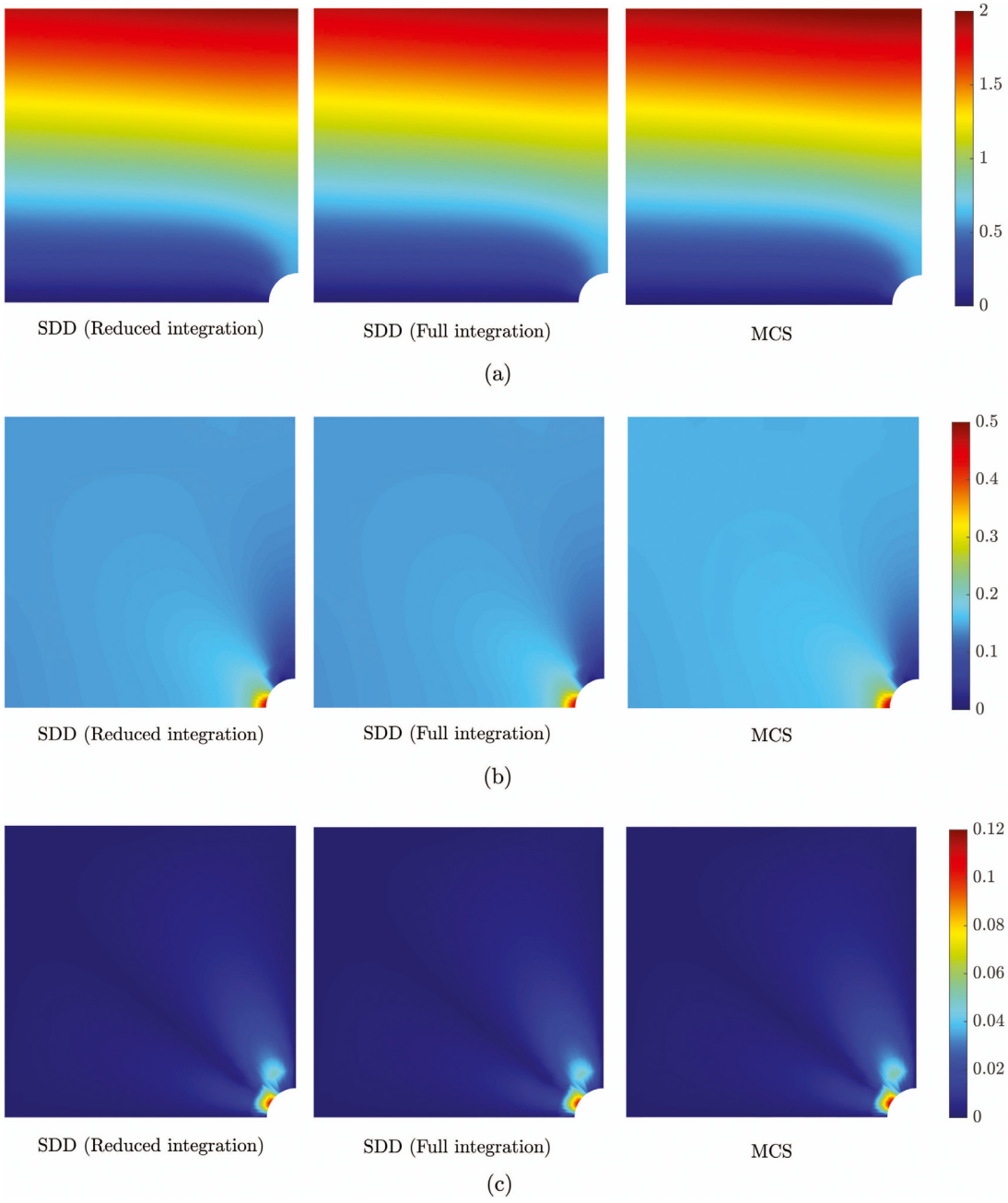

Fig. 11. Contour plots for the standard deviation of (a) u_y, (b) σ_y, and (c) $|\tau_{xy}|$ obtained by SDD with reduced integration by DRI (left), SDD with full integration (middle), and MCS (right) in consistent units in Example 3.

the more refined the knot vectors representing the stochastic domain of B-splines, the more crucial the need for DRI becomes in the corresponding computations. This further magnifies the benefit and convenience of the DRI technique proposed.

Note that, in this example, the lognormal probability measure corresponding to σ_∞ was transformed to a uniform probability measure for the SDD method to be theoretically applicable, as mentioned in Section 2.2. Although the

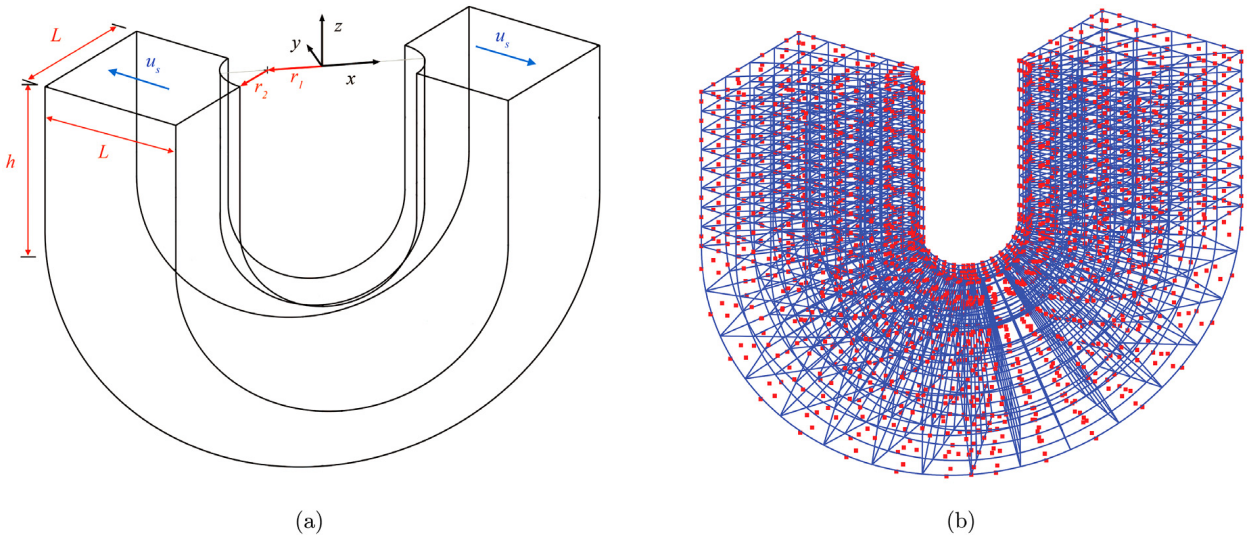

Fig. 12. A horseshoe under asymmetric loading in Example 4: (a) problem schematic; (b) refined mesh employed in the analyses. The control points are illustrated by red closed squares.

target distribution with a bounded domain is not unique, since only one of the random variables was unbounded, mapping to the uniform distribution led to accurate results, at least for the calculation of second-moment properties of the response. Thus, there was no need to try other target distributions.

5.4. Example 4: Horseshoe random field problem

Having studied the positive impact of the DRI on a two-dimensional physical domain, the final example delves into a geometrically complex yet single-patch three-dimensional horseshoe problem with a high-dimensional random input. The solid horseshoe is constructed by executing a U-sweep of the cross section of a notched square. The cross section has a size $L \times L$, subtracted by a quarter disk with the radius r_2, as shown in Fig. 12(a). Additional parameters required to completely describe the horseshoe geometry, namely, r_1 representing the distance between the origin and the centerpoint of the quarter disk and h identifying the height of the straight portion, are also sketched. The following values were used: $r_1 = 3$ units, $r_2 = 4$ units, $L = 20$ units, and $h = 20$ units. Hence, the geometry is completely defined.

For material properties, the Poisson's ratio $\nu = 1/3$. Moreover, the Young's modulus $E(\mathbf{z}; \cdot)$ is a homogeneous lognormal random field with mean $\mu_E = 210 \times 10^9$ units and coefficient of variation $v_E = 0.1$. As a translation random field, $E(\mathbf{z}; \cdot)$ is written as

$$E(\mathbf{z}; \cdot) = C_\alpha \exp[\alpha(\mathbf{z}; \cdot)],$$

where

$$C_\alpha = \frac{\mu_E}{\sqrt{1 + v_E^2}}$$

and $\alpha(\mathbf{z}; \cdot)$ is a homogeneous Gaussian random field with mean *zero* and covariance function

$$\Gamma(\mathbf{z}, \mathbf{z}') = \sigma^2 \exp\left(-\frac{||\mathbf{z} - \mathbf{z}'||}{bL}\right), \quad \mathbf{z}, \mathbf{z}' \in \mathcal{D} \subset \mathbb{R}^3$$

with $\sigma^2 = 0.01$ and $b = 1$.

For stress analysis, the top surfaces of the horseshoe are subjected to displacements of magnitude $u_s = 0.01$ units in the directions shown in Fig. 12(a). This causes asymmetric deformation and resultant twisting of the horseshoe.

The stochastic problem requires calculating the statistical properties and probabilistic characteristics of stresses and strains due to uncertain material properties.

Employing IGA with quadratic NURBS, the geometry was constructed precisely. Similar to the procedure in Example 3, a base eight-element mesh was generated with quadratic NURBS; the corresponding knot vectors are reported in Table C.3, and in Fig. C.1 of Appendix C. Too numerous to report, the control points and weights corresponding to the coarse mesh have been suppressed. The fine mesh illustrated in Fig. 12(b) was then constructed by simple knot insertion, which consists of 1024 quadratic elements and 2442 control points. The control points are depicted by red closed squares. Readers interested in modeling techniques of three-dimensional objects via NURBS are directed to the book by Cottrell et al. [30].

The random field describing Young's modulus was discretized by the K–L expansion, exploiting the isogeometric collocation method [43] and considering a total of 15 ($N = N' = 15$) independent standard Gaussian random variables. As the 15th eigenvalue was only 2.47% percent of the first eigenvalue, this number was deemed adequate to satisfactorily approximate the random field. The domain discretization and NURBS objects, such as orders and knot vectors, for the K–L expansion and deterministic IGA were identical. The eigenpairs $\{\lambda_i, \phi_i(\mathbf{z})\}$, $i = 1, \ldots, N$, were then numerically calculated. By dint of the collocation method, the random field is efficiently discretized with adequate accuracy. However, the error due to the truncation of the K–L expansion is not studied here. The horseshoe problem was solved by crude MCS and SDD. For the SDD method, each standard Gaussian random variable X_i was transformed to a truncated Gaussian variable, where the original PDF was truncated at $x_i = \pm 3$. Both univariate and bivariate SDD approximations with $p = 1$ and $p = 2$ and two or four subintervals ($I = 2$ or 4) were employed. The expansion coefficients were calculated using the DRI technique with $p + 2$ Gauss points on each subinterval. Two sets of stochastic analyses were performed for this example, the results of which are presented next.

5.4.1. Second-moment analysis

The first set of analyses entails the evaluation of the second-moment properties of a stress and a strain component. The crude MCS was chosen to provide the benchmark solution along with two SDD methods: univariate, quadratic SDD approximation ($S = 1$, $p = 2$) and bivariate, quadratic SDD approximation ($S = 2$, $p = 2$), each with two subintervals ($I = 2$). Figs. 13 and 14 demonstrate the contour plots of the mean and standard deviation, respectively, of the normal stress σ_z and the shear strain ϵ_{xz}, obtained by the univariate SDD, bivariate SDD, and MCS. No tangible improvement is noticed when implementing bivariate SDD over univariate SDD, indicating that the original function is dominantly univariate with weak interaction terms. Furthermore, both methods satisfactorily estimate the mean and standard deviation of the responses in comparison with those obtained from the MCS to the extent that any differences in the contours are barely distinguishable. The error in the maximum values of the mean and standard deviation of stress and strain committed by SDD are below 0.5%. Moreover, the numbers of function evaluations for the univariate SDD and bivariate SDD are 121 and 6841, respectively. This reveals that the univariate, quadratic ($S = 1$, $p = 2$) SDD approximation with two subintervals is adequate for computation of the second-moment properties of the responses with only 121 IGA. For even more accurate results, further refinement and an increase in the B-splines orders is valid for SDD. However, doing so for this high-dimensional problem will be numerically intensive, especially for the bivariate SDD approximation. Although DRI significantly contributes to the numerical scheme developed, there is still a need to further improve on the numerical integration methods for high-dimensional integrals involving splines.

5.4.2. Probability distribution analysis

In this section, the CDF of a relevant stress component at a critical point of the horseshoe is studied. Let the point at which the mean of the normal stress σ_z is maximum be the critical point and denote by $\sigma_{z,c}$ the normal stress at that point. For CDF analysis, the crude MCS was selected along with three univariate SDD methods: univariate, linear SDD approximation with two subintervals ($S = 1$, $p = 1$, $I = 2$); univariate, linear SDD approximation with four subintervals ($S = 1$, $p = 1$, $I = 4$); and univariate, quadratic SDD approximation with two subintervals ($S = 1$, $p = 2$, $I = 2$). With each SDD surrogate obtained, one is able to re-sample the SDD approximation with a relatively large sample size – 10^5 in this example – to estimate the CDF of $\sigma_{z,c}$.

Fig. 15 illustrates the CDF of $\sigma_{z,c}$ calculated by the aforementioned methods. Evidently, the univariate, quadratic SDD approximation with two subintervals not only assiduously captures the second-moment statistical properties of the response, as observed previously, but also provides an impressive approximation of the CDF with only 121 IGA, compared to 10^4 IGA in the case of MCS.

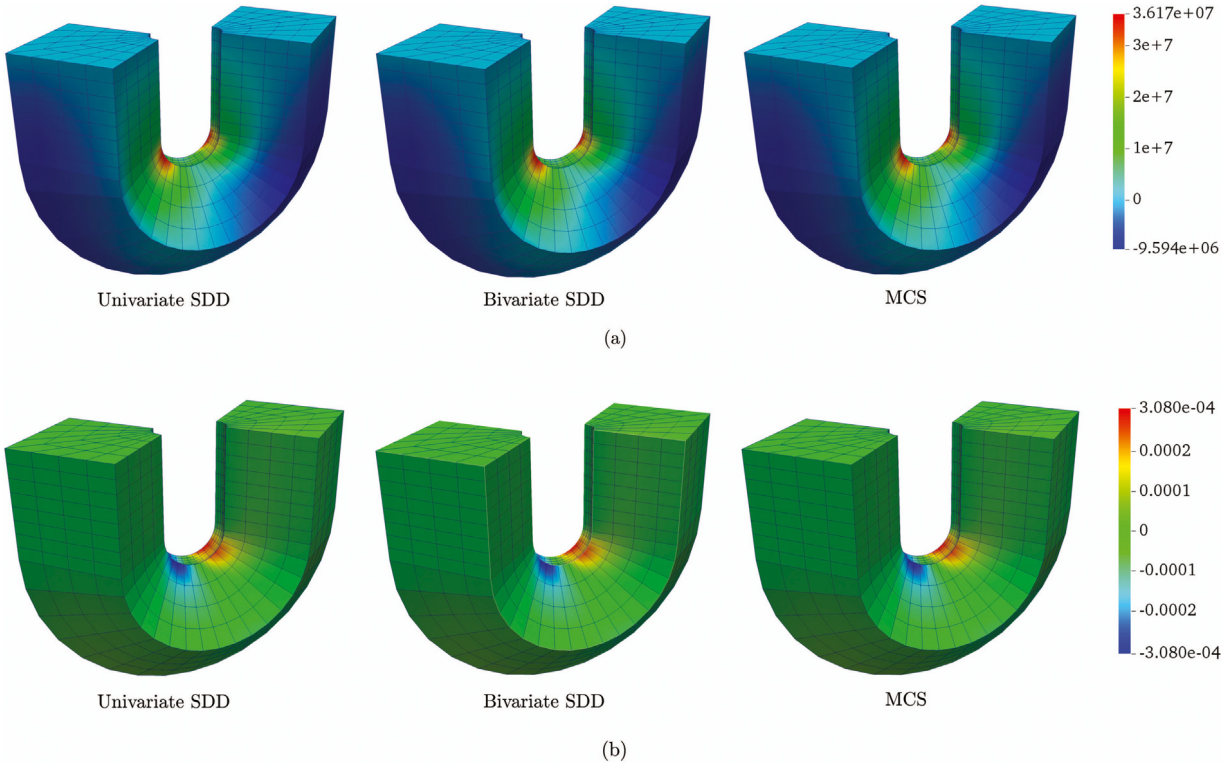

Fig. 13. Contour plots for the mean of (a) normal stress σ_z and (b) shear strain ϵ_{xz} obtained by univariate SDD (left), bivariate SDD (middle); and MCS (right) in consistent units in Example 4.

Now the question to be addressed is whether the lower-order SDD methods are also able to accurately estimate the distribution of $\sigma_{z,c}$. According to Fig. 15, while the linear SDD approximation with two subintervals and 91 IGA struggles to approximate the CDF of $\sigma_{z,c}$ well, increasing the number of subintervals from two to four helps remarkably. However, the number of IGA is nearly doubled from 91 to 181, and yet, the linear SDD with four subintervals is not as good as the quadratic SDD with two subintervals in either accuracy or efficiency.

Note that the transformation of the Gaussian probability measures to other desired probability measures may change the results. However, a transformation yielding the least difference in the original and mapped distributions is more enticing, since in general, heavily nonlinear transformations are to be avoided to obtain better approximations. Investigations revealed that, for the fourth numerical example, transformation from Gaussian to truncated Gaussian measures indeed provided much more accurate yet numerically affordable results than mapping them to uniform probability measures. For brevity, the results corresponding to uniform mapping are not reported here. Evidently, the SDD method can reliably estimate the statistical characteristics and probability distribution of a random response for bounded or unbounded distributions, while the geometrically complex domains are precisely modeled in IGA.

6. Outlook

Although the development of SDD–IGA contributes to the advancement of SIGA and to overall progress in stochastic mechanics, there are a few open questions or concerns. The computationally intensive high-dimensional integration involved in calculating the expansion coefficients remains to be conquered as the most challenging part of the SDD method. For the K–L expansion in random field discretization and for the Galerkin IGA in linear elasticity, the integrals are at most three-dimensional since they are defined on a physical domain, whereas in the stochastic domain, in practice, the number of random variables often exceeds 10 and may even be 100 or more. This issue, however, was alleviated to some extent by introducing the DRI technique. Fundamentally, the problem of high-dimensional integration is not specific to SDD or SIGA. Obviously, there is a long-standing interest and need for further research in this direction.

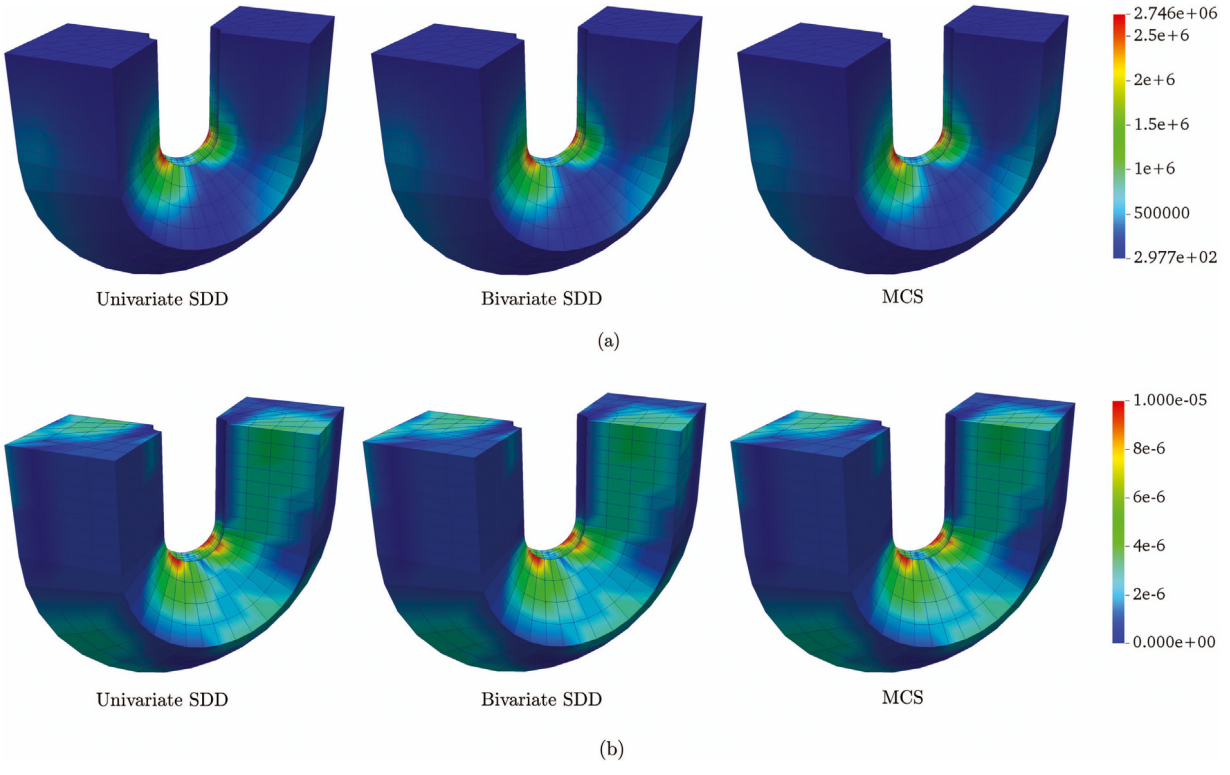

Fig. 14. Contour plots for the standard deviation of (a) normal stress σ_z and (b) shear strain ϵ_{xz} obtained by univariate SDD (left), bivariate SDD (middle); and MCS (right) in consistent units in Example 4.

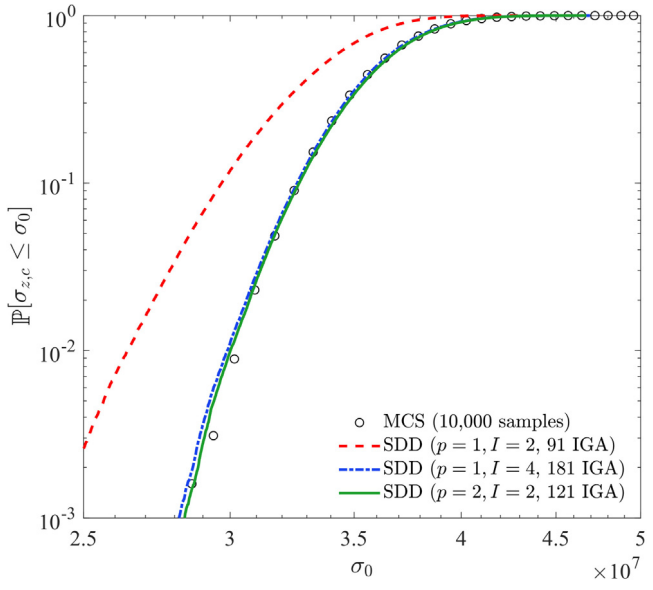

Fig. 15. The CDF of the response $\sigma_{z,c}$ in Example 4.

Another open question in SDD–IGA is the choice of the knot vectors and B-spline orders. It was observed in the second example that having a knot in the proximity of the nonsmoothness of the original response function may help with the accurate approximation of the response function, provided that the order is chosen cleverly. Hence, seeking optimal or adaptive knot vectors and B-spline orders would be a significant contribution to this area. This also presents the opportunity to introduce unbounded knot vectors to the established framework to handle unbounded distributions of random input. If that were done, no measure transformation would be required.

Last but not least, the scope of the proposed SDD–IGA method, in the context of SIGA, should be expanded to account for more complex multi-patch geometries in IGA in the future.

7. Conclusion

A new stochastic method, referred to as SDD–IGA, was developed for solving stochastic boundary-value problems from linear elasticity. As a stochastic version of the Galerkin isogeometric analysis, the method has at least two important novelties. First, measure-consistent orthonormal B-splines were employed for refining ADD of a high-dimensional response function. The result is a Fourier-like orthogonal expansion in spline basis, which is equipped to capture locally abrupt changes in stochastic responses, including discontinuity and nonsmoothness, better than globally supported polynomial basis. Second, an innovative DRI technique, meant for computing high-dimensional integrals, was exploited for estimating the expansion coefficients of SDD–IGA. Consequently, high-dimensional stochastic problems, featuring locally prominent, highly nonlinear response functions, can be effectively solved with a polynomial computational complexity. Therefore, a time-honored stochastic problem associated with the curse of dimensionality has been diminished to an appreciable magnitude. Analytical formulae were derived to calculate the second-moment properties of a general SDD–IGA approximation. The significance of the SDD–IGA method lies in harnessing common ingredients of IGA – B-splines and NURBS – in geometrical modeling, random field discretization, stress analysis, and now UQ for any square-integrable output random variable of interest. Because of the connection to IGA, the SDD–IGA method preserves exact geometrical representation of commonly used shapes found in engineering, thereby removing an additional source of imprecision in the discretization process.

A numerical example entailing functions with harsh regularities illustrates the dominance of SDD over PCE and sparse grids methods. Moreover, the numerical results from three elastostatic problems, including a three-dimensional, fifteen-variable horseshoe problem, demonstrate that a low-order SDD–IGA approximation is capable of efficiently delivering probabilistic solutions with an approximation quality as good as, if not better than, that obtained from a high-order PDD–IGA method. The established SDD–IGA framework is most suitable in the presence of locally nonlinear or nonsmooth response behavior, not uncommon in engineering applications.

Appendix A. Isogeometric analysis

The IGA was developed to establish a tight connection between CAD and FEA, where the B-splines and NURBS are employed for both frameworks [30]. This section describes the basic concepts of IGA and its notations for single-patch geometries, which is sufficient for the materials covered in this paper.

A.1. Univariate basis functions

B-splines are constructed via knot vectors and orders.[4] A knot vector $\boldsymbol{\xi}_k$ in coordinate direction $k \in \mathbb{N}$ and of order $p_k \in \mathbb{N}_0$ is defined on a bounded interval $[a_k, b_k] \subset \mathbb{R}$ with $a_k < b_k$ and $n_k > p_k \geq 0$ as a non-decreasing sequence of real numbers as

$$\boldsymbol{\xi}_k := \{\xi_{k,i_k}\}_{i_k=1}^{n_k+p_k+1} = \{a_k = \xi_{k,1}, \xi_{k,2}, \ldots, \xi_{k,n_k+p_k+1} = b_k\},$$
$$\xi_{k,1} \leq \xi_{k,2} \leq \cdots \leq \xi_{k,n_k+p_k+1}$$

where $n_k \in \mathbb{N}$ represents the number of basis functions in direction k. Here, the coordinate direction k corresponds to either the stress analysis or the K–L expansion ($k = 1, \ldots, d$), where $d = 1, 2, 3$, or the stochastic analysis ($k = 1, \ldots, N$) with $N \in \mathbb{N}$ being the dimension of the stochastic problem. Moreover, ξ_{k,i_k} is the i_kth knot with $i_k = 1, 2, \ldots, n_k + p_k + 1$ identifying its index. There are $n_k + p_k + 1$ knots in the knot vector, which may be

[4] *Degree* and *order* are used interchangeably in the paper.

equally spaced or unequally spaced, resulting in a uniform or non-uniform mesh, respectively. More importantly, a knot may be repeated $1 \leq m_{k,i_k} \leq p_k + 1$ times, where m_{k,i_k} is referred to as its multiplicity. The multiplicity has significant impact on the regularity of B-spline functions. In case of r_k distinct knots in $\boldsymbol{\xi}_k$ with corresponding multiplicities $m_{k,1}, \ldots, m_{k,r_k}$, the general expression of the knot vector in direction k reduces to

$$\boldsymbol{\xi}_k = (a_k = \underbrace{\zeta_{k,1}, \ldots, \zeta_{k,1}}_{m_{k,1} \text{ times}}, \underbrace{\zeta_{k,2}, \ldots, \zeta_{k,2}}_{m_{k,2} \text{ times}}, \ldots, \underbrace{\zeta_{k,r_k}, \ldots, \zeta_{k,r_k}}_{m_{k,r_k} \text{ times}} = b_k),$$

which comprises

$$\sum_{i_k=1}^{r_k} m_{k,i_k} = n_k + p_k + 1.$$

knots. For any occurrence $\zeta_{k,i_k} > \zeta_{k,i_k-1}$, denote by $[\zeta_{k,i_k-1}, \zeta_{k,i_k}] \subset \mathbb{R}$ a subinterval of the domain $[a_k, b_k]$. A knot vector is called open if its first and last knots appear $p_k + 1$ times [55]. Only open knot vectors are employed in this work.

With a specified knot vector $\boldsymbol{\xi}_k$ and order p_k in coordinate direction k, the B-spline function $B^k_{i_k,p_k,\boldsymbol{\xi}_k}(x_k)$ with $i_k = 1, \ldots, n_k$ is generated in a recursive manner. The *zero*-order basis function is formed by

$$B^k_{i_k,0,\boldsymbol{\xi}_k}(x_k) = \begin{cases} 1, & \zeta_{k,i_k} \leq x_k < \zeta_{k,i_k+1}, \\ 0, & \text{otherwise}, \end{cases}$$

and higher-order B-splines are all generated by the Cox–de Boor formula [46]

$$B^k_{i_k,p_k,\boldsymbol{\xi}_k}(x_k) = \frac{x_k - \zeta_{k,i_k}}{\zeta_{k,i_k+p_k} - \zeta_{k,i_k}} B^k_{i_k,p_k-1,\boldsymbol{\xi}_k}(x_k) + \frac{\zeta_{k,i_k+p_k+1} - x_k}{\zeta_{k,i_k+p_k+1} - \zeta_{k,i_k+1}} B^k_{i_k+1,p_k-1,\boldsymbol{\xi}_k}(x_k), \tag{A.1}$$

where $0/0$ is considered as *zero*.

The B-spline functions possess several beneficial properties. They are non-negative, locally supported on the interval, linearly independent, and committed to partition of unity [28]. A B-spline is also everywhere pointwise C^∞-continuous except at the knots ζ_{k,i_k} of multiplicity m_{k,i_k}, where it is $C^{p_k - m_{k,i_k}}$-continuous, provided that $1 \leq m_{k,i_k} < p_k + 1$. Some of these properties are quite fruitful in computational stress analysis, random field discretization, and stochastic analysis.

A.2. Multivariate functions for stress and K–L analyses

Multivariate B-splines in d variables with knot vectors $\boldsymbol{\xi}_1, \ldots, \boldsymbol{\xi}_d$ are constructed from the tensor product of the corresponding univariate B-splines. Define three multi-indices $\mathbf{i} := (i_{k_1}, \ldots, i_{k_d}) \in \mathbb{N}^d$, $\mathbf{p} := (p_{k_1}, \ldots, p_{k_d}) \in {\mathbb{N}_0}^d$, and $\boldsymbol{\Xi} := (\boldsymbol{\xi}_1, \ldots, \boldsymbol{\xi}_d)$. For the first multi-index, denote by

$$\mathcal{I} := \left\{\mathbf{i} = (i_{k_1}, \ldots, i_{k_d}) : 1 \leq i_{k_l} \leq n_{k_l},\ l = 1, \ldots, d\right\} \subset \mathbb{N}^d$$

a multi-index set. Denoting by $\hat{\mathcal{D}}$ the parametric space, for $\mathbf{i} \in \mathcal{I}$ and $\mathbf{p}$, the multivariate B-spline function $\mathrm{B}_{\mathbf{i},\mathbf{p},\boldsymbol{\Xi}} : \hat{\mathcal{D}} \to \mathbb{R}$ is defined as

$$\mathrm{B}_{\mathbf{i},\mathbf{p},\boldsymbol{\Xi}}(\mathbf{x}) := \prod_{k=1}^{d} B^k_{i_k,p_k,\boldsymbol{\xi}_k}(x_k)$$

with the corresponding tensor-product B-spline space

$$\mathcal{B}_h := \bigotimes_{k=1}^{d} \mathcal{B}_k(p_k; \boldsymbol{\xi}_k) = \bigotimes_{k=1}^{d} \mathrm{span}\{B^k_{i_k,p_k,\boldsymbol{\xi}_k}(x_k)\}_{i_k=1,\ldots,n_k} = \mathrm{span}\{\mathrm{B}_{\mathbf{i},\mathbf{p},\boldsymbol{\Xi}}(\mathbf{x})\}_{\mathbf{i}\in\mathcal{I}}.$$

$\mathcal{B}_h$ is therefore a family of piecewise polynomials that, due to the tensor-product structure, inherit the basic properties of their univariate counterparts. Denote by $\mathbb{R}^+$ the collection of all positive real numbers and by $w_{\mathbf{i}} \in \mathbb{R}^+$ a positive weight. Then, a weight function $w : \hat{\mathcal{D}} \to \mathbb{R}$ can be defined through a linear combination of multivariate B-splines as [56]

$$w(\mathbf{x}) := \sum_{\mathbf{i}\in\mathcal{I}} w_{\mathbf{i}} \mathrm{B}_{\mathbf{i},\mathbf{p},\boldsymbol{\Xi}}(\mathbf{x}).$$

Hence, the multivariate NURBS function $\mathrm{R}_{\mathbf{i},\mathbf{p},\boldsymbol{\Xi}}(\mathbf{x}) : \hat{\mathcal{D}} \to \mathbb{R}$ is defined as [30]

$$\mathrm{R}_{\mathbf{i},\mathbf{p},\boldsymbol{\Xi}}(\mathbf{x}) \coloneqq \frac{w_{\mathbf{i}}\mathrm{B}_{\mathbf{i},\mathbf{p},\boldsymbol{\Xi}}(\mathbf{x})}{w(\mathbf{x})} = \frac{w_{\mathbf{i}}\mathrm{B}_{\mathbf{i},\mathbf{p},\boldsymbol{\Xi}}(\mathbf{x})}{\sum_{\mathbf{i}\in\mathcal{I}} w_{\mathbf{i}}\mathrm{B}_{\mathbf{i},\mathbf{p},\boldsymbol{\Xi}}(\mathbf{x})}, \tag{A.2}$$

producing the NURBS function space

$$\mathcal{R}_h \coloneqq \mathrm{span}\{\mathrm{R}_{\mathbf{i},\mathbf{p},\boldsymbol{\Xi}}(\mathbf{x})\}_{\mathbf{i}\in\mathcal{I}}. \tag{A.3}$$

The NURBS functions also inherit the important properties from their piecewise polynomial counterparts.

For each $\mathbf{i} \in \mathcal{I}$, let $\mathbf{c}_{\mathbf{i}} \in \mathbb{R}^d$ be a control point. Denote by $n_c \coloneqq |\mathcal{I}|$ the cardinality of $\mathcal{I}$, representing the number of such control points for any d-dimensional geometry. Call the collection of such control points $\{\mathbf{c}_{\mathbf{i}}\}_{\mathbf{i}\in\mathcal{I}}$ a control mesh. Using NURBS functions, the physical domain $\mathcal{D} \subset \mathbb{R}^d$ is obtained by a geometrical mapping $\mathbf{x} : \hat{\mathcal{D}} \to \mathcal{D} \subset \mathbb{R}^d$, which is described more explicitly by

$$\mathbf{H}(\mathbf{x}) = \sum_{\mathbf{i}\in\mathcal{I}} \mathrm{R}_{\mathbf{i},\mathbf{p},\boldsymbol{\Xi}}(\mathbf{x})\mathbf{c}_{\mathbf{i}}, \tag{A.4}$$

which can be a line, a surface, or a volume. Where the control points are and how they are weighted determines the geometry in a convenient manner. The use of NURBS by (A.2) is vital in many engineering applications where the geometry may not be accurately modeled via B-splines. Using the geometrical mapping (A.4), the physical mesh $\mathcal{K}_h$ is the projection of the parametric mesh $\mathcal{Z}_h$, that is,

$$\mathcal{K}_h \coloneqq \{K = \mathbf{H}(Z) : Z \in \mathcal{Z}_h\},$$

where element K of the physical mesh is the image of element Z of the parametric discretization. Moreover, define the space of NURBS functions in the physical domain $\mathcal{D}$ as the push-forward of the NURBS space $\mathcal{R}_h$ in (A.3) via

$$\mathcal{V}_h \coloneqq \mathrm{span}\left\{\mathrm{R}_{\mathbf{i},\mathbf{p},\boldsymbol{\Xi}} \circ \mathbf{H}^{-1}\right\}_{\mathbf{i}\in\mathcal{I}} = \mathrm{span}\left\{\bar{\mathrm{R}}_{\mathbf{i},\mathbf{p},\boldsymbol{\Xi}}\right\}_{\mathbf{i}\in\mathcal{I}}, \tag{A.5}$$

where $\bar{\mathrm{R}}_{\mathbf{i},\mathbf{p},\boldsymbol{\Xi}} \coloneqq \mathrm{R}_{\mathbf{i},\mathbf{p},\boldsymbol{\Xi}} \circ \mathbf{H}^{-1}$ is the NURBS function in the physical domain.

The accuracy of IGA depends on the enrichment of the NURBS spaces $\mathcal{R}_h$ in (A.3) and $\mathcal{V}_h$ in (A.5) via refinement. Although many conic geometries may be exactly represented by a single element, mesh refinement is often needed for numerical accuracy purposes when solving a PDE. A simple and straightforward type of refinement is through knot insertion, which is equivalent to the h-refinement commonly used in FEM. Here, an obvious difference between the two is the continuity in the bases of the former over the element boundaries. However, the regularity of the NURBS functions may be altered by repeating knots as desired. By knot insertion, a finer mesh is constructed by subsequently adding knots to the existing knot vectors without changing the geometry. It yields an increase in the number of control points and thus in the number of basis functions. As an example, consider inserting a new knot $\zeta'_k \in [\zeta_{k,l}, \zeta_{k,l+1})$, $1 \le l \le n_k + p_k$, to the existing knot vector $\boldsymbol{\xi}_k \coloneqq (\zeta_{k,1}, \zeta_{k,2}, \ldots, \zeta_{k,n_k+p_k+1})$. The Cox–de Boor formula in (A.1) is then applied to the new knot vector

$$\boldsymbol{\xi}'_k \coloneqq (\zeta'_{k,1}, \zeta'_{k,2}, \ldots, \zeta'_{k,n_k+p_k+2}) = (\zeta_{k,1}, \zeta_{k,2}, \ldots, \zeta_{k,l}, \zeta'_k, \zeta_{k,l+1}, \ldots, \zeta_{k,n_k+p_k+1}).$$

Hence, a new set of $n_k + 1$ basis functions is created with their span nesting the span of existing basis functions, and, for a NURBS object in $\mathbb{R}^d$, a new set of control points should be defined for the new basis functions to obtain an object that is geometrically and parametrically the same as the original one. More details of the isogeometric analysis are suppressed for brevity. Readers interested in this topic are directed to [30] and [31].

Appendix B. Examples of SDD coefficients with DRI

This section presents some examples of the expansion coefficients in SDD, where the DRI is implemented. The examples entail $S = R = 1$, $S = R = 2$, and $S = R = 3$. The conditions on the summations noted by $u \subseteq v$ in (35) are also imposed. This will filter out some of the terms with zero contributions due to (17) and (18).

$\underline{S = R = 1.}$

$$\hat{y}_{\emptyset} = \sum_{k=1}^{N} \int_{\mathbb{A}^{\{k\}}} y(c_1, \ldots, c_{k-1}, x_k, c_{k+1}, \ldots, c_N) f_{X_k}(x_k) dx_k - (N-1) y(\mathbf{c})$$
$$\hat{\alpha}_{ki_k} = \int_{\mathbb{A}^{\{k\}}} y(c_1, \ldots, c_{k-1}, x_k, c_{k+1}, \ldots, c_N) \psi^{k}_{i_k, p_k, \boldsymbol{\xi}_k}(x_k) f_{X_k}(x_k) dx_k$$

$\underline{S = R = 2.}$

$$\begin{aligned}
\hat{y}_{\emptyset} &= \sum_{k_1=1}^{N-1} \sum_{k_2=k_1+1}^{N} \int_{\mathbb{A}^{\{k_1,k_2\}}} y(c_1, \ldots, c_{k_1-1}, x_{k_1}, c_{k_1+1}, \ldots, c_{k_2-1}, x_{k_2}, c_{k_2+1}, \ldots, c_N) \times \\
&\quad f_{X_{k_1}}(x_{k_1}) f_{X_{k_2}}(x_{k_2}) dx_{k_1} dx_{k_2} - (N-2) \sum_{k=1}^{N} \int_{\mathbb{A}^{\{k\}}} y(c_1, \ldots, c_{k-1}, x_k, c_{k+1}, \ldots, c_N) f_{X_k}(x_k) dx_k \\
&\quad + \frac{(N-1)(N-2)}{2} y(\mathbf{c}) \\
\hat{\alpha}_{ki_k} &= \sum_{\substack{k_1=1 \\ \{k\} \subset \{k_1,k_2\}}}^{N-1} \sum_{k_2=k_1+1}^{N} \int_{\mathbb{A}^{\{k_1,k_2\}}} y(c_1, \ldots, c_{k_1-1}, x_{k_1}, c_{k_1+1}, \ldots, c_{k_2-1}, x_{k_2}, c_{k_2+1}, \ldots, c_N) \psi^{k}_{i_k, p_k, \boldsymbol{\xi}_k}(x_k) \times \\
&\quad f_{X_{k_1}}(x_{k_1}) f_{X_{k_2}}(x_{k_2}) dx_{k_1} dx_{k_2} - (N-2) \int_{\mathbb{A}^{\{k\}}} y(c_1, \ldots, c_{k-1}, x_k, c_{k+1}, \ldots, c_N) \psi^{k}_{i_k, p_k, \boldsymbol{\xi}_k}(x_k) \times \\
&\quad f_{X_k}(x_k) dx_k \\
\hat{\beta}_{k_1 k_2 i_{k_1} i_{k_2}} &= \int_{\mathbb{A}^{\{k_1,k_2\}}} y(c_1, \ldots, c_{k_1-1}, x_{k_1}, c_{k_1+1}, \ldots, c_{k_2-1}, x_{k_2}, c_{k_2+1}, \ldots, c_N) \psi^{k_1}_{i_{k_1}, p_{k_1}, \boldsymbol{\xi}_{k_1}}(x_{k_1}) \times \\
&\quad \psi^{k_2}_{i_{k_2}, p_{k_2}, \boldsymbol{\xi}_{k_2}}(x_{k_2}) f_{X_{k_1}}(x_{k_1}) f_{X_{k_2}}(x_{k_2}) dx_{k_1} dx_{k_2}
\end{aligned}$$

$\underline{S = R = 3.}$

$$\begin{aligned}
\hat{y}_{\emptyset} &= \sum_{k_1=1}^{N-2} \sum_{k_2=k_1+1}^{N-1} \sum_{k_3=k_2+1}^{N} \int_{\mathbb{A}^{\{k_1,k_2,k_3\}}} y(c_1, \ldots, c_{k_1-1}, x_{k_1}, c_{k_1+1}, \ldots, c_{k_2-1}, x_{k_2}, c_{k_2+1}, \ldots, c_{k_3-1}, x_{k_3}, c_{k_3+1}, \ldots, c_N) \\
&\quad \times f_{X_{k_1}}(x_{k_1}) f_{X_{k_2}}(x_{k_2}) f_{X_{k_3}}(x_{k_3}) dx_{k_1} dx_{k_2} dx_{k_3} \\
&\quad - (N-3) \sum_{k_1=1}^{N-1} \sum_{k_2=k_1+1}^{N} \int_{\mathbb{A}^{\{k_1,k_2\}}} y(c_1, \ldots, c_{k_1-1}, x_{k_1}, c_{k_1+1}, \ldots, c_{k_2-1}, x_{k_2}, c_{k_2+1}, \ldots, c_N) \\
&\quad \times f_{X_{k_1}}(x_{k_1}) f_{X_{k_2}}(x_{k_2}) dx_{k_1} dx_{k_2} + \frac{(N-2)(N-3)}{2} \\
&\quad \times \sum_{k=1}^{N} \int_{\mathbb{A}^{\{k\}}} y(c_1, \ldots, c_{k-1}, x_k, c_{k+1}, \ldots, c_N) f_{X_k}(x_k) dx_k - \frac{(N-1)(N-2)(N-3)}{6} y(\mathbf{c}) \\
\hat{\alpha}_{ki_k} &= \sum_{k_1=1}^{N-2} \sum_{\substack{k_2=k_1+1 \\ \{k\} \subset \{k_1,k_2,k_3\}}}^{N-1} \sum_{k_3=k_2+1}^{N} \int_{\mathbb{A}^{\{k_1,k_2,k_3\}}} y(c_1, \ldots, c_{k_1-1}, x_{k_1}, c_{k_1+1}, \ldots, c_{k_2-1}, x_{k_2}, c_{k_2+1}, \ldots, c_{k_3-1}, x_{k_3}, c_{k_3+1}, \ldots, c_N) \\
&\quad \times \psi^{k}_{i_k, p_k, \boldsymbol{\xi}_k}(x_k) f_{X_{k_1}}(x_{k_1}) f_{X_{k_2}}(x_{k_2}) f_{X_{k_3}}(x_{k_3}) dx_{k_1} dx_{k_2} dx_{k_3} \\
&\quad - (N-3) \sum_{\substack{k_1=1 \\ \{k\} \subset \{k_1,k_2\}}}^{N-1} \sum_{k_2=k_1+1}^{N} \int_{\mathbb{A}^{\{k_1,k_2\}}} y(c_1, \ldots, c_{k_1-1}, x_{k_1}, c_{k_1+1}, \ldots, c_{k_2-1}, x_{k_2}, c_{k_2+1}, \ldots, c_N) \psi^{k}_{i_k, p_k, \boldsymbol{\xi}_k}(x_k) \\
&\quad \times f_{X_{k_1}}(x_{k_1}) f_{X_{k_2}}(x_{k_2}) dx_{k_1} dx_{k_2} \\
&\quad + \frac{(N-2)(N-3)}{2} \int_{\mathbb{A}^{\{k\}}} y(c_1, \ldots, c_{k-1}, x_k, c_{k+1}, \ldots, c_N) \psi^{k}_{i_k, p_k, \boldsymbol{\xi}_k}(x_k) f_{X_k}(x_k) dx_k
\end{aligned}$$

$$
\begin{aligned}
\hat{\beta}_{k_1k_2i_{k_1}i_{k_2}} &= \sum_{j_1=1}^{N-2}\sum_{j_2=j_1+1}^{N-1}\sum_{j_3=j_2+1}^{N}\int_{\mathbb{A}^{\{j_1,j_2,j_3\}}} y(c_1,\ldots,c_{j_1-1},x_{j_1},c_{j_1+1},\ldots,c_{j_2-1},x_{j_2},c_{j_2+1},\ldots,c_{j_3-1},x_{j_3},c_{j_3+1},\ldots,c_N)\\
&\quad \{k_1,k_2\}\subset\{j_1,j_2,j_3\}\\
&\quad \times\psi^{j_1}_{i_{j_1},p_{j_1},\boldsymbol{\xi}_{j_1}}(x_{j_1})\psi^{j_2}_{i_{j_2},p_{j_2},\boldsymbol{\xi}_{j_2}}(x_{j_2})f_{X_{j_1}}(x_{j_1})f_{X_{j_2}}(x_{j_2})f_{X_{j_3}}(x_{j_3})dx_{j_1}dx_{j_2}dx_{j_3}\\
&\quad -(N-3)\int_{\mathbb{A}^{\{k_1,k_2\}}} y(c_1,\ldots,c_{k_1-1},x_{k_1},c_{k_1+1},\ldots,c_{k_2-1},x_{k_2},c_{k_2+1},\ldots,c_N)\\
&\quad \times\psi^{k_1}_{i_{k_1},p_{k_1},\boldsymbol{\xi}_{k_1}}(x_{k_1})\psi^{k_2}_{i_{k_2},p_{k_2},\boldsymbol{\xi}_{k_2}}(x_{k_2})f_{X_{k_1}}(x_{k_1})f_{X_{k_2}}(x_{k_2})dx_{k_1}dx_{k_2}\\
\hat{\gamma}_{k_1k_2k_3i_{k_1}i_{k_2}i_{k_3}} &= \int_{\mathbb{A}^{\{k_1,k_2,k_3\}}} y(c_1,\ldots,c_{k_1-1},x_{k_1},c_{k_1+1},\ldots,c_{k_2-1},x_{k_2},c_{k_2+1},\ldots,c_{k_3-1},x_{k_3},c_{k_3+1},\ldots,c_N)\\
&\quad \times\psi^{k_1}_{i_{k_1},p_{k_1},\boldsymbol{\xi}_{k_1}}(x_{k_1})\psi^{k_2}_{i_{k_2},p_{k_2},\boldsymbol{\xi}_{k_2}}(x_{k_2})\psi^{k_3}_{i_{k_3},p_{k_3},\boldsymbol{\xi}_{k_3}}(x_{k_3})f_{X_{k_1}}(x_{k_1})f_{X_{k_2}}(x_{k_2})f_{X_{k_3}}(x_{k_3})\\
&\quad \times dx_{k_1}dx_{k_2}dx_{k_3}
\end{aligned}
$$

Appendix C. IGA details of numerical examples

Supplementary information about the isogeometric analyses in the numerical examples is provided in this section. NURBS objects for Example 2 are listed in Table C.1. Table C.2 lists the control points corresponding to the coarse mesh in Example 3. Moreover, Fig. C.1 demonstrates the coarse meshes for Example 3 and Example 4, for which the knot vectors are presented in Table C.3. The directions of the knot vectors are also defined in Fig. C.1 and the control points are illustrated by red closed squares. For Example 4, the control points are too many to list and are thus omitted.

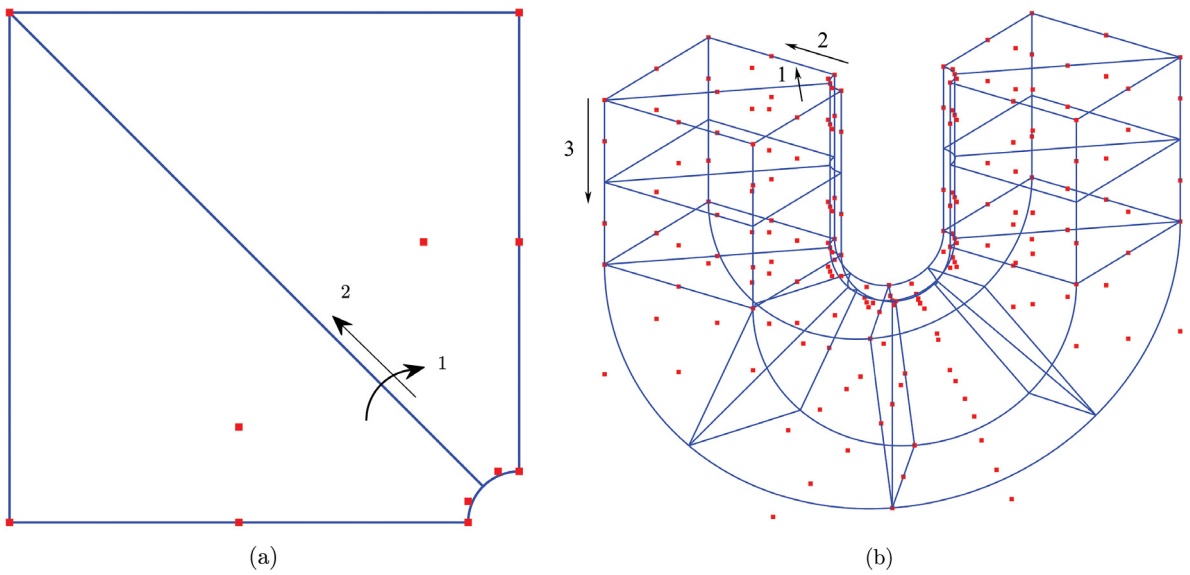

Fig. C.1. Coarse mesh discretization and knot vector directions for (a) Example 3 and (b) Example 4. The control points are illustrated by red closed squares.

Table C.1
NURBS objects for the isogeometric analysis in Example 2.

Control points	Weights	Knot vector
{0, 1.5, 3, 4.5, 6}	{1, 1, 1, 1, 1}	$\boldsymbol{\xi}_z = \{0, 0, 0, 1/3, 2/3, 1, 1, 1\}$

Table C.2
Control points and weights corresponding to the base mesh for the isogeometric analysis in Example 3.

Control point coordinates	Weight
$(-a, 0)$	1
$(-0.5L - 0.5a, 0)$	0.85355
$(-L, 0)$	0.85355
$(-a, (\sqrt{2}-1)a)$	1
$(-0.5L - 0.5a, 0.1875L)$	1
$(-L, L)$	1
$(-(\sqrt{2}-1)a, a)$	1
$(-0.1875L, 0.5L + 0.5a)$	1
$(-L, L)$	1
$(0, a)$	1
$(0, 0.5L + 0.5a)$	1
$(0, L)$	1

Table C.3
Knot vectors corresponding to the base mesh for the isogeometric analyses in Examples 3 and 4[a].

Example 3	Example 4
$\boldsymbol{\xi}_1 = \{0, 0, 0, 0.5, 1, 1, 1\}$	$\boldsymbol{\xi}_1 = \{0, 0, 0, 0.5, 0.5, 1, 1, 1\}$
$\boldsymbol{\xi}_2 = \{0, 0, 0, 1, 1, 1\}$	$\boldsymbol{\xi}_2 = \{0, 0, 0, 1, 1, 1\}$
	$\boldsymbol{\xi}_3 = \{0, 0, 0, 0.25, 0.25, 0.5, 0.5, 0.75, 0.75, 1, 1, 1\}$

[a]Directions are defined in Fig. C.1.

References

[1] M. Papadrakakis, V. Papadopoulos, Robust and efficient methods for stochastic finite element analysis using Monte Carlo simulation, Comput. Methods Appl. Mech. Engrg. 134 (1996) 325–340.

[2] R.E. Caflisch, Monte Carlo and quasi-Monte Carlo methods, Acta Numer. 7 (1998) 1–49.

[3] R.G. Ghanem, P.D. Spanos, Stochastic Finite Elements: A Spectral Approach, Springer, Berlin, 1991.

[4] G. Stefanou, The stochastic finite element method: Past, present and future, Comput. Methods Appl. Mech. Engrg. 198 (2009) 1031–1051.

[5] M.K. Deb, I.M. Babuška, J.T. Oden, Solution of stochastic partial differential equations using Galerkin finite element techniques, Comput. Methods Appl. Mech. Engrg. 190 (2001) 6359–6372.

[6] H.G. Matthies, A. Keese, Galerkin methods for linear and nonlinear elliptic stochastic partial differential equations, Comput. Methods Appl. Mech. Engrg. 194 (2005) 1295–1331.

[7] M. Berveiller, B. Sudret, M. Lemaire, Stochastic finite element: a non intrusive approach by regression, Eur. J. Comput. Mech. 15 (2006) 81–92.

[8] M. Kamiński, Generalized perturbation-based stochastic finite element method in elastostatics, Comput. Struct. 85 (2007) 586–594.

[9] M. Kamiński, Application of the generalized perturbation-based stochastic boundary element method to the elastostatics, Eng. Anal. Bound. Elem. 31 (2007) 514–527.

[10] A. Nouy, A generalized spectral decomposition technique to solve a class of linear stochastic partial differential equations, Comput. Methods Appl. Mech. Engrg. 196 (2007) 4521–4537.

[11] A. Nouy, Generalized spectral decomposition method for solving stochastic finite element equations: Invariant subspace problem and dedicated algorithms, Comput. Methods Appl. Mech. Engrg. 197 (2008) 4718–4736.

[12] F. Xiong, S. Greene, W. Chen, A new sparse grid based method for uncertainty propagation, Struct. Multidiscip. Optim. 41 (2010) 335–349.

[13] I. Kaljevič, S. Saigal, Stochastic boundary elements in elastostatics, Comput. Methods Appl. Mech. Engrg. 109 (1993) 259–280.

[14] R. Honda, Stochastic BEM with spectral approach in elastostatic and elastodynamic problems with geometrical uncertainty, Eng. Anal. Bound. Elem. 29 (2005) 415–427.

[15] S. Rahman, B.N. Rao, A perturbation method for stochastic meshless analysis in elastostatics, Internat. J. Numer. Methods Engrg. 50 (2001) 1969–1991.

[16] S. Rahman, H. Xu, A meshless method for computational stochastic mechanics, Int. J. Comput. Methods Eng. Sci. Mech. 6 (2005) 41–58.

[17] N. Wiener, The homogeneous chaos, Amer. J. Math. 60 (4) (1938) 897–936.

[18] D. Xiu, G.E. Karniadakis, The Wiener–Askey polynomial chaos for stochastic differential equations, SIAM J. Sci. Comput. 24 (2002) 619–644.

[19] X. Wan, G. Karniadakis, An adaptive multi-element generalized polynomial chaos method for stochastic differential equations, J. Comput. Phys. 209 (2005) 617–642.
[20] J. Foo, X. Wan, G. Karniadakis, The multi-element probabilistic collocation method (ME-PCM): error analysis and applications, J. Comput. Phys. 227 (2008) 9572–9595.
[21] S. Rahman, Approximation errors in truncated dimensional decompositions, Math. Comp. 83 (290) (2014) 2799–2819.
[22] C. Su, S. Zhao, Stochastic spline fictitious boundary element method in elastostatics problems with random fields, Eng. Anal. Bound. Elem. 36 (2012) 759–771.
[23] M. Motamed, F. Nobile, A stochastic collocation method for the second order wave equation with a discontinuous random speed, Numer. Math. 123 (2013) 493–536.
[24] I. Babuška, M. Motamed, R. Tempone, A stochastic multiscale method for the elastodynamic wave equation arising from fiber composites, Comput. Methods Appl. Mech. Engrg. 276 (2014) 190–211.
[25] X.B. Hu, X.Y. Cui, H. Feng, G.Y. Li, Stochastic analysis using the generalized perturbation stable node-based smoothed finite element method, Eng. Anal. Bound. Elem. 70 (2016) 40–55.
[26] A. Gupta, C.O. Arun, Stochastic meshfree method for elastic buckling analysis of columns, Comput. Struct. 194 (2018) 32–47.
[27] H. Xu, S. Rahman, A generalized dimension-reduction method for multidimensional integration in stochastic mechanics, Internat. J. Numer. Methods Engrg. 61 (2004) 1992–2019.
[28] T.J.R. Hughes, J.A. Cottrell, Y. Bazilevs, Isogeometric analysis: CAD, finite elements, NURBS, exact geometry and mesh refinement, Comput. Methods Appl. Mech. Engrg. 194 (2005) 4135–4195.
[29] J.A. Cottrell, T.J.R. Hughes, A. Reali, Studies of refinement and continuity in isogeometric structural analysis, Comput. Methods Appl. Mech. Engrg. 196 (2007) 4160–4183.
[30] J.A. Cottrell, T.J.R. Hughes, Y. Bazilevs, Isogeometric Analysis: Toward Integration of CAD and FEA, John Wiley & Sons, 2009.
[31] V.P. Nguyen, C. Anitescu, S.P.A. Bordas, T. Rabczuk, Isogeometric analysis: An overview and computer implementation aspects, Comput. Methods Appl. Mech. Engrg. 199 (2010) 264–275.
[32] Y. Bazilevs, L. Beirao de Veiga, J. Cottrell, T.J.R. Hughes, G. Sangalli, Isogeometric analysis: approximation, stability and error estimates for h-refined meshes, Math. Models Methods Appl. Sci. 16 (2006) 1031–1090.
[33] Y. Bazilevs, V.M. Calo, J.A. Cottrell, J.A. Evans, T.J.R. Hughes, S. Lipton, M.A. Scott, T.W. Sederberg, Isogeometric analysis using T-splines, Comput. Methods Appl. Mech. Engrg. 199 (2010) 229–263.
[34] M.R. Dörfel, B. Jüttler, B. Simeon, Adaptive isogeometric analysis by local h-refinement with T-splines, Comput. Methods Appl. Mech. Engrg. 199 (2010) 264–275.
[35] S. Rahman, A polynomial dimensional decomposition for stochastic computing, Internat. J. Numer. Methods Engrg. 76 (2008) 2091–2116.
[36] J. Mason, G. Rodriguez, S. Seatzu, Orthogonal splines based on B-splines – with applications to least squares, smoothing and regularisation problems, Numer. Algorithms 5 (1993) 25–40.
[37] T.D. Hien, H. Noh, Stochastic isogeometric analysis of free vibration of functionally graded plates considering material randomness, Comput. Methods Appl. Mech. Engrg. 318 (2017) 845–863.
[38] K. Li, W. Gao, D. Wu, C. Song, T. Chen, Spectral stochastic isogeometric analysis of linear elasticity, Comput. Methods Appl. Mech. Engrg. 332 (2018) 157–190.
[39] J. Beck, L. Tamellini, R. Tempone, IGA-based multi-index stochastic collocation for random PDEs on arbitrary domains, Comput. Methods Appl. Mech. Engrg. 351 (2019) 330–350.
[40] S. Rahman, R. Jahanbin, A spline dimensional decomposition for uncertainty quantification, Numer. Math. (2019) submitted for publication.
[41] M. Loève, Probability Theory, Vol. II, Springer, Berlin, Heidelberg, New York, 1977.
[42] S. Rahman, A Galerkin isogeometric method for Karhunen–Loève approximation of random fields, Comput. Methods Appl. Mech. Engrg. 338 (2018) 533–561.
[43] R. Jahanbin, S. Rahman, An isogeometric collocation method for efficient random field discretization, Int. J. Numer. Methods Eng. 117 (3) (2019) 344–369.
[44] T.J.R. Hughes, The Finite Element Method: Linear Static and Dynamic Finite Element Analysis, Dover Publications, 2000.
[45] B. Efron, C. Stein, The jackknife estimate of variance, Ann. Statist. 9 (3) (1981) 586–596.
[46] C. De Boor, On calculation with B-splines, J. Approx. Theory 6 (1972) 50–62.
[47] H. Rabitz, O. Alis, General foundations of high dimensional model representations, J. Math. Chem. 25 (1999) 197–233.
[48] M. Griebel, M. Holtz, Dimension-wise integration of high-dimensional functions with applications to finance, J. Complexity 26 (5) (2010) 455–489.
[49] W. Gautschi, Orthogonal Polynomials: Computation and Approximation, Oxford University Press, New York, 2004.
[50] H. Xu, S. Rahman, Decomposition methods for structural reliability analysis, Probab. Eng. Mech. 20 (2005) 239–250.
[51] S. Rahman, Mathematical properties of polynomial dimensional decomposition, SIAM/ASA J. Uncertain. Quantif. 6 (2018) 816–844.
[52] A. Genz, A. Malik, An adaptive algorithm for numerical integration over an n-dimensional rectangular region, J. Comput. Appl. Math. 6 (1980) 295–302.
[53] S. Smolyak, Quadrature and interpolation formulas for tensor products of certain classes of functions, Dokl. Akad. Nauk SSSR 148 (1963) 1042–1045.
[54] T. Gerstner, M. Griebel, Numerical integration using sparse grids, Numer. Algorithms 18 (1998) 209–232.
[55] L.A. Piegl, W. Tiller, The NURBS Book, second ed., Springer-Verlag, Berlin, 1997.
[56] G.E. Farin, NURBS Curves and Surfaces: From Projective Geometry to Practical Use, A. K. Peters, Ltd., Natick, MA, 1999.